# Estimation of thermal properties and boundary heat transfer coefficient of the ground with a Bayesian technique

Zhanat Karashbayeva, Julien Berger, Helcio R.B. Orlande, Marie-Hélène Azam

# Estimation of thermal properties and boundary heat transfer coefficient of the ground with a Bayesian technique

Zhanat Karashbayeva [a, b*], Julien Berger[a], Helcio R.B. Orlande[c], Marie-Hélène Azam[d]

[a] Laboratoire des Sciences de l'Ingénieur pour l'Environnement (LaSIE), UMR 7356 CNRS, La Rochelle Université, CNRS, 17000, La Rochelle, France
[b] Astana IT University, Astana, Kazakhstan
[c] POLI/COPPE, Mechanical Engineering Department, Federal University of Rio de Janeiro
[d] Université de Strasbourg, INSA Strasbourg, CNRS, ICube Laboratory UMR 7357, Equipe GCE, Strasbourg, France
*corresponding author, e-mail address : zhanat.karashbaeva@astanait.edu.kz

**Abstract**

Urbanization is a key contributor for climate change. Increasing urbanization rate causes an urban heat island (UHI) effect, which strongly depends on the short- and long-wave radiative transfer between the surfaces. In order to accurately calculate radiative fluxes, it is required to assess the ground surface temperature which depends on the thermal properties and the surface heat transfer coefficient in the heat transfer problem. The aim of this paper is to estimate the thermal properties of the ground and the time varying surface heat transfer coefficient by solving an inverse problem. The DUFORT–FRANKEL scheme is applied for solving the unsteady heat transfer forward problem, under the assumption of no water mass transfer. For the inverse problem, a MARKOV chain Monte Carlo method is used to estimate the posterior probability density of unknown parameters within the BAYESIAN framework of statistics, by applying the METROPOLIS–HASTINGS algorithm for random sample generation. Actual temperature measurements available at different ground depths were used for the solution of the inverse problem. Different time discretizations were examined for the transient heat transfer coefficient at the ground surface, which then involved different prior distributions. Results of different case studies show that the estimated values of the unknown parameters were in accordance with literature values. Moreover, with the present solution of the inverse problem the temperature residuals were smaller than those obtained by using standard values for the unknown parameters.

**Key words:** inverse heat transfer problem; BAYESIAN approach; surface heat transfer coefficient; urban ground; thermal properties of the ground.

## 1 Introduction

As recently reported, the global urbanization rate is above 50% and it is predicted to increase in the future. Urbanization is becoming one of the main causes of global warming. Current studies indicate that the urban heat island (UHI) phenomenon is rapidly increasing in the areas with higher urbanization rates [1, 2]. The heat flux from ground is one of the main reasons for the development of the UHI effect. As reported in [3], pavements and ground are crucial for effective mitigation strategies to ensure lower surface temperature and reduce urban heat island effects. Ground heat flux is the most important component of the surface energy balance [4–7]. Therefore, accurate computational simulations of heat transfer processes in the ground are of great importance for the prediction of UHI effects [8–10]. For the mathematical modeling, thermal properties of the ground, such as thermal conductivity and volumetric heat capacity, are key parameters for energy balances [11, 12]. Consequently, it is very important to accurately know those properties. Moreover, the boundary conditions of the physical model play an important role, especially at the surface of the ground [13]. Energy balance at the surface of the ground is composed of different heat flux components. According to [14], convective heat transfer modeled by NEWTON's law of cooling can have a significant impact on the surface temperature.

Accurate values of the thermophysical properties of the pavement materials, as well as of the heat transfer coefficient at the surface of the ground, are needed for numerical simulations to analyze or predict the UHI phenomenon[15]. Some studies available in the literature were dedicated to the direct measurement of parameters appearing in models for the ground heat transfer, but with destructive and/or expensive methods [16–19]. Inverse problems can also be used for the identification of model parameters and functions using *in-situ* ground measurements. However, inverse problems are inherently ill-posed and highly affected by measurement and modelling errors. Consequently, most of the available works devoted to the estimation of the thermal properties of the ground are based on simulated measurements with hypothetical errors [20, 21] or controlled laboratory experiments [22–24]. Inverse problems utilizing *in-situ* ground measurements obtained in real field experiments were dealt with by our group, for the estimation of a constant thermal diffusivity [25] and of a spatially-varying thermal diffusivity [26]. In these cases, the inverse problems were solved through the minimization of a maximum likelihood objective functional with Bayesian inferences [25] or gradient-based methods [26]. Moreover, available works mostly consider the surface heat transfer coefficient as constant [27], despite the fact that such quantity varies in time due to different effects, including the wind velocity and direction over the surface. In [28], a time-dependent heat transfer coefficient was estimated, but with simulated measurements. An analysis of the state-of-the-art shows that the simultaneous estimation of the ground thermal properties and of a time varying surface heat transfer coefficient with real *in-situ* measured data is still open.

Therefore, the objective of this work is to apply a Bayesian approach for simultaneously estimating the thermal conductivity, volumetric heat capacity and time varying surface heat transfer coefficient of ground, using actual field temperature measurements at different depths below the surface [29]. This paper is structured as follows: Section 2 describes the physical model. Section 3 gives information about the inverse problem method and the algorithm used for its solution. In Section 4, three case studies are investigated where the ground thermal conductivity, volumetric heat capacity and time varying surface heat transfer coefficient are retrieved. A comparison at the urban scale is performed between a standard simulation and one using the parameters and functions estimated in this work in Section 5. This section is then followed by the conclusions obtained in this work.

# 2 Methodology

## 2.1 Description of Physical Model

The physical problem considers one-dimensional transient heat conduction in ground defined by the spatial domain $\Omega_x = [0, L]$, where $L$ $[\mathsf{m}]$ is the ground depth and $\Omega_t = [0, t_f]$ is the time domain, where $t_f$ $[\mathsf{s}]$ is the time horizon for investigating the phenomena. By neglecting moisture transfer effects, the physical problem can be formulated as [30]:

$$C \frac{\partial T}{\partial t} = \frac{\partial}{\partial x}\left(\kappa \frac{\partial T}{\partial x}\right), \tag{1}$$

where $C = \rho c_p$ $[\mathsf{J \cdot m^{-3} \cdot K^{-1}}]$ is the volumetric heat capacity, $\rho$ $[\mathsf{kg \cdot m^{-3}}]$ is the density, $c_p$ $[\mathsf{J \cdot kg^{-1} \cdot K^{-1}}]$ is the specific heat, $\kappa$ $[\mathsf{W \cdot m^{-1} \cdot K^{-1}}]$ is the thermal conductivity, and $T$ $[\mathsf{K}]$ is the temperature of the ground depending on spatial $x$ and time $t$ variables.

The boundary condition at the surface of the ground defines the balance between diffusive, radiation and convection fluxes. It is expressed as:

$$\kappa \frac{\partial T}{\partial x} = h(t)\,(T - T_\infty(t)) - q_\infty(t), \qquad \forall t \in \Omega_t, \qquad x = 0, \tag{2}$$

where $T_\infty$ $[\mathsf{K}]$ is the temperature of the surrounding air, $q_\infty$ $[\mathsf{W \cdot m^{-2}}]$ is the net radiation flux and $h(t)$ $\left[\mathsf{W} \cdot \mathsf{m}^{-2} \cdot \mathsf{K}^{-1}\right]$ is the surface heat transfer coefficient, which are time-dependent functions due to climate variations.

At the depth $x = L$, a DIRICHLET boundary condition is set:

$$T \;=\; T_g(t), \qquad \forall t \in \Omega_t\,, \qquad x \;=\; L\,. \tag{3}$$

The initial condition is:

$$T \;=\; T_{in}(x), \qquad \forall x \in \Omega_x\,, \qquad t \;=\; 0\,. \tag{4}$$

The physical model is illustrated in Figure 1.

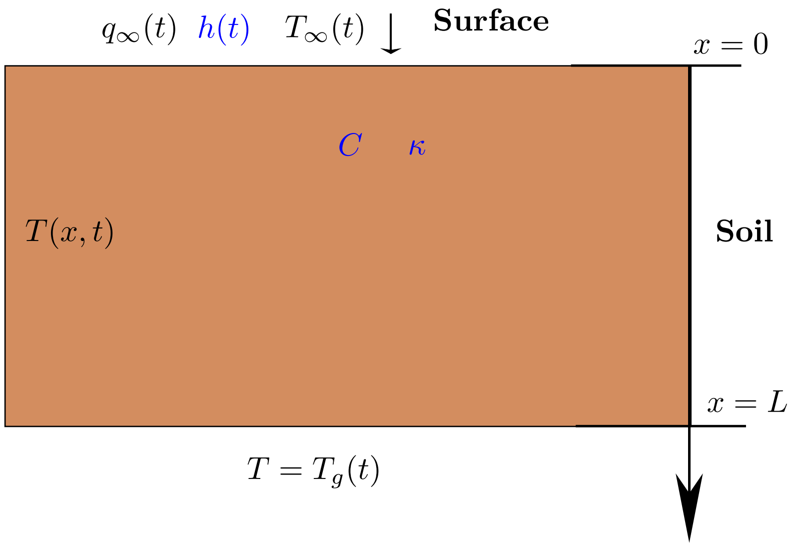


Figure 1. *Illustration of the physical model.*

Equations (1) to (4) define the direct or forward problem, so that the distribution of temperature $T(x,t)$ can be computed when the physical properties, initial and boundary conditions are known. The direct problem is solved in dimensionless form using DUFORT–FRANKEL scheme [31], implemented in Matlab.

## 3 Inverse Problem via Bayesian inference

The inverse problem aims at the estimation of the thermal conductivity ($\kappa$), surface heat transfer coefficient ($h(t)$) and volumetric heat capacity ($C$). Since the ground is assumed homogeneous, the thermal conductivity and volumetric heat capacity coefficients are considered as constants. However, the surface heat transfer coefficient is assumed depending on time and defined as:

$$h(t) \;=\; \sum_{i=1}^{N_t} h_i\ \eta_i(t), \tag{5}$$

where $\eta_i$ is the piecewise basis function:

$$\eta_i(t) \;=\; \begin{cases} 1\,, & t_i \leq t \leq t_{i+1}\,, \quad \forall i \;\in\; \{\,1\,,\,\ldots\,,\,N_t\,\} \\ 0\,, & \text{otherwise.} \end{cases} \tag{6}$$

The unknown parameters $\mathbf{P} \in \Omega_P$ are denoted by:

$$\mathbf{P} \stackrel{\text{def}}{:=} (p_1\,, p_2\,, p_3\,, p_4\,, \ldots, p_N) \equiv (\kappa\,, C\,, h_1\,, h_2\,, \ldots, h_{N_t})\,,$$

where $N = 2 + N_t$ is the number of unknowns. For the solution of the inverse problem, transient temperature measurements taken at different depths of the ground are given. The temperature measurements are denoted as $\mathbf{Y}$. The measurement errors are supposed as uncorrelated GAUSSIAN random variables, with zero means and known variances. The measurement errors are additive and independent of the unknown parameters $\mathbf{P}$.

### 3.1 Sensitivity coefficients

It is important to analyze the sensitivity coefficients before attempting to solve the parameter estimation problem, in order to evaluate the identifiability of the unknowns. The sensitivity coefficient is defined by:

$$X_{p_{ij}} = \frac{\partial T}{\partial p_j}\Big|_{x\,=\,x_i}\,, \qquad \forall (\,i\,,\,j\,) \in \{\,1\,,\,\ldots\,,\,M\,\} \times \{\,1\,,\,\ldots\,,\,N\,\}\,, \tag{7}$$

where $i$ stands for the measurement positions. Different approaches exist for the computation of sensitivity coefficients [32]. In our case, the central finite-difference approximation is used,

$$X_{p_{ij}} \approx \frac{T(x_i\,, t\,, p_1\,, p_2\,, \ldots, p_j + \Delta p_j\,, \ldots, p_N) - T(x_i\,, t\,, p_1\,, p_2\,, \ldots, p_j - \Delta p_j\,, \ldots, p_N)}{2\,\Delta p_j}\,, \tag{8}$$

where $\Delta\, p_j \,=\, 10^{-2}\, p_j$ in our computations. The convergence of the above finite-difference approximation of the sensitivity coefficients was verified by also using $\Delta p_j = \{10^{-1} p_j\,, 10^{-3} p_j\,, 10^{-4} p_j\}$.

### 3.2 Bayesian estimation

The MARKOV Chain Monte Carlo (MCMC) method is applied to estimate the posterior distribution of the unknown parameters within the BAYESIAN framework of statistics [33, 34]. According to BAYES' theorem, we have [34–37]:

$$\pi_{posterior}(\mathbf{P}) = \pi(\mathbf{P}|\mathbf{Y}) = \frac{\pi(\mathbf{P})\pi(\mathbf{Y}|\mathbf{P})}{\pi(\mathbf{Y})}\,, \tag{9}$$

where $\pi_{posterior}(\mathbf{P})$ is the posterior probability density, $\pi(\mathbf{P})$ is the prior density, $\pi(\mathbf{Y}|\mathbf{P})$ is the likelihood function, and $\pi(\mathbf{Y})$ is the marginal probability density of the measurements. The latter is generally difficult to estimate and not required from a practical point of view to determine the unknown parameters. Given that, BAYES' theorem is simplified to:

$$\pi(\mathbf{P}|\mathbf{Y}) \propto \pi(\mathbf{P})\pi(\mathbf{Y}|\mathbf{P})\,. \tag{10}$$

With the above hypotheses regarding the measurement errors, the likelihood is expressed as [34, 38, 39]:

$$\pi(\mathbf{Y}|\mathbf{P}) = (2\,\pi)^{-D/2}|\mathbf{W}|^{-1/2} \exp\left(-\frac{1}{2}[\mathbf{Y} - \mathbf{T}(\mathbf{P})]^T \mathbf{W}^{-1}[\mathbf{Y} - \mathbf{T}(\mathbf{P})]\right) \tag{11}$$

where $D$ is the total number of measurements, and $\mathbf{T}(\mathbf{P})$ is the solution of the direct problem (1) - (4), obtained at the each sensor position and with given parameters $\mathbf{P}$.

Two different prior probability densities are examined in this work. One of them is a GAUSSIAN distribution in the domain $\Omega_P$:

$$\pi(\mathbf{P}) = (2\,\pi)^{-N/2}|\mathbf{V}|^{-1/2} \exp\left\{-\frac{1}{2}[\mathbf{P} - \boldsymbol{\mu}]^T \mathbf{V}^{-1}[\mathbf{P} - \boldsymbol{\mu}]\right\}\,, \tag{12}$$

where $\boldsymbol{\mu}$ and $\mathbf{V}$ are the known mean and covariance matrix of the prior, respectively. As the parameters are assumed independent, the prior covariance matrix is diagonal, with elements given by the variances, $\sigma_m^2$, that is,

$$[\mathbf{V}_{m,n}] \; = \; \begin{cases} \sigma_m^2\,, & m = n\,, \qquad \forall(\,m\,,\,n\,) \,\in\, \{\,1\,,\,\ldots\,,\,N\,\}^{\,2}\,, \\ 0\,, & \text{otherwise.} \end{cases} \tag{13}$$

The other prior density is the Gaussian smoothness prior, which is extremely useful for estimating parameters that approximate local values of smooth functions [34]. In this work the Gaussian smoothness prior is only applied for the surface heat transfer coefficient $h(t)$, Equation (5). It is given in the following form:

$$\pi(\mathbf{P}) = (2\,\pi)^{-N_t/2}\gamma^{N_t/2}|\mathbf{Z}^{-1}|^{-1/2}\exp\left\{-\frac{1}{2}\gamma\mathbf{P}^T\,\mathbf{Z}\,\mathbf{P}\right\}\,, \tag{14}$$

where $\mathbf{Z} = \mathbf{D}^T\mathbf{D}$ and $\mathbf{D}$ is a $(\mathbf{I}-1)\times\mathbf{I}$ first-order difference matrix given in next form:

$$\mathbf{D} = \begin{bmatrix} -1 & 1 & 0 & \ldots & 0 \\ 0 & -1 & 1 & \ldots & 0 \\ \ldots & \ldots & \ldots & \ldots & \ldots \\ 0 & \ldots & 0 & -1 & 1 \end{bmatrix},$$

and the parameter $\gamma$ is treated in this work as a hyperparameter, that is, an unknown parameter of the model of the posterior distribution. In this work, we consider the hyperparameter density in the form of a Rayleigh distribution [34]:

$$\pi(\gamma) = \frac{\gamma}{\gamma_0^2}\exp\left[-\frac{1}{2}\left(\frac{\gamma}{\gamma_0}\right)^2\right]\,, \tag{15}$$

where $\gamma_0\,[\,\mathsf{m}^4\cdot\mathsf{K}^2\cdot\mathsf{W}^{-2}\,]$ is the scale parameter and it is defined by user.

The Metropolis–Hastings algorithm is used in this work to explore the posterior distribution. The implementation of this algorithm starts with the selection of a proposal distribution $q(\mathbf{P}^*|\mathbf{P}^{(k)})$, which is used to draw a new candidate sample $\mathbf{P}^*$ given the current sample $\mathbf{P}^{(k)}$ of the Markov chain (Step 2:). Here, a uniform proposal is used:

$$q(\mathbf{P}^*|\mathbf{P}^{(k)}) = \mathbf{P}^{(k)} + \omega\,\mathbf{W}([-1\,,1]), \tag{16}$$

where $\omega$ is the maximum step that can be taken from $\mathbf{P}^{(k)}$ to generate $\mathbf{P}^*$. Then, the solution of the direct problem, Equations (1) - (4), is computed given the sampled parameter $\mathbf{P}^*$ (Step 3:). After that, the posterior distribution is evaluated together with the acceptance factor defined by:

$$\alpha(\mathbf{P}^*|\mathbf{P}^{(k)}) = \min\left[1, \frac{\pi_{posterior}(\mathbf{P}^*)\,q(\mathbf{P}^{(k)}|\mathbf{P}^*)}{\pi_{posterior}(\mathbf{P}^{(k)})\,q(\mathbf{P}^*|\mathbf{P}^{(k)})}\right]. \tag{17}$$

A random value W uniformly distributed on $[0,1]$ is then generated (Step 5:). At Step 6:, if $W \le \alpha(\mathbf{P}^*|\mathbf{P}^{(k)})$ the candidate parameter is retained, $\mathbf{P}^{(k+1)} = \mathbf{P}^*$. Otherwise, set $\mathbf{P}^{(k+1)} = \mathbf{P}^{(k)}$. A sequence of sampled parameters is then obtained $\{\mathbf{P}^{(1)}\,,\mathbf{P}^{(2)}\,,\ldots,\mathbf{P}^{(N_s)}\}$. The Metropolis–Hastings algorithm can be summarized in the following steps [34, 36, 39]:

1. Let $k = 0$ and start the Markov chain with sample $\mathbf{P}^{(0)}$ at the initial state.
2. Sample a candidate point $\mathbf{P}^*$ from a proposal distribution $q(\mathbf{P}^*|\mathbf{P}^{(k)})$.
3. Compute the direct problem solution from Equations (1) - (4).
4. Calculate the probability $\alpha(\mathbf{P}^*|\mathbf{P}^{(k)})$ with Equation (17).
5. Generate a random value $W \sim \mathcal{U}(0,1)$, which is uniformly distributed in $(0,1)$.
6. If $W \leq \alpha(\mathbf{P}^*|\mathbf{P}^{(k)})$, set $\mathbf{P}^{(k+1)} = \mathbf{P}^*$. Otherwise, set $\mathbf{P}^{(k+1)} = \mathbf{P}^{(k)}$.
7. Make $k = k+1$ and return to step 2 in order to generate the sequence $\{\mathbf{P}^{(1)}, \mathbf{P}^{(2)}, \ldots, \mathbf{P}^{(N_s)}\}$.

# 4 Case study

## 4.1 Description

The experimental data were provided by [29], from experiments in a parking lot located in the Université Gustave Eiffel (former IFSTTAR Institute), Bouguenais, France. The parking lot structure was composed of a 5 $\mathsf{cm}$ thick layer of asphalt concrete pavement over a ballast layer. The total area of the parking lot was 50 $\mathsf{m}$ by 50 $\mathsf{m}$. Due to the small thickness of the asphalt layer as compared to other dimensions of the parking lot region analyzed, the heat conduction problem was formulated as one-dimensional in a homogeneous region with depth $L = 5$ $\mathsf{cm}$. Thermocouples were installed to measure the temperature inside the asphalt layer at $x_m \in \{0, 1, 2, 3, 4\}$ $\mathsf{cm}$. Measurements of the air temperature and ground temperature at $x = L = 5$ $\mathsf{cm}$ were used for the boundary conditions (2)–(3) of the direct problem, respectively. Their time variations given as $T_\infty(t)$ and $T_g(t)$, respectively, are shown in Figure 2(a). In boundary condition (2), $q_\infty(t)$ corresponds to the net radiation value, which was measured by a net radiometer - NRlite (Kipp & Zonen) [29], is presented in Figure 2(b). In the experiment, the radiation heat flux and the air temperature were measured at 1 $\mathsf{m}$ above surface. Moreover, the wind velocity was measured using a YOUNG sensor at 1.5 $\mathsf{m}$ above the surface. Figure 2(c) presents these measurements of the wind velocity. As it can be seen in this figure, the wind velocity varied during the experiment, thus requiring that the surface heat transfer coefficient be considered as a time dependent function. Regarding the initial condition given in Figure 2(d), it was obtained by interpolating the values of temperatures at each measurement position at $t = 0$.

The initial experiments from [29] were performed with a duration of 144 $\mathsf{h}$ (on June 6 - 12, 2004) in a parking lot of 2500 $\mathsf{m}^2$ flat bare asphalt square. During the whole measurement period, one natural rain was observed on June 10, and short drizzles on June 8 and 9. Since the phase change of moisture was not taken into account in the mathematical model, and no measurement of moisture content were carried out during the experimental campaign, the estimation procedure was performed up to $t_f = 28$ $\mathsf{h}$ (just before the first rain event).

For all cases of parameter estimation, the transient measurements of the sensors located at $x_m \in \{0, 1, 2, 3, 4\}$ $\mathsf{cm}$ are used in the calculation of the likelihood function. In addition, in the Bayesian inversion the likelihood function accounts for the measurement uncertainty of $\sigma_{meas} = 0.1°C$ at each measurement point. It should be noted that the experimental error was assumed to be independent and normally distributed.

## 4.2 Practical identifiability

The reduced sensitivity coefficients were computed at each of the 5 sensor locations. Due to the nonlinear character of the present parameter estimation problem, the analysis of the sensitivity coefficients is local and based on reference values for the model parameters. From the literature review, the following values for the volumetric heat capacity and thermal conductivity of dry asphalt concrete were considered [40]: $C = 2.1$ $\mathsf{MJ \cdot m^{-3} \cdot K^{-1}}$ and $\kappa = 2.23$ $\mathsf{W \cdot m^{-1} \cdot K^{-1}}$, respectively. Values of the surface heat transfer coefficients corresponding to mild natural con-

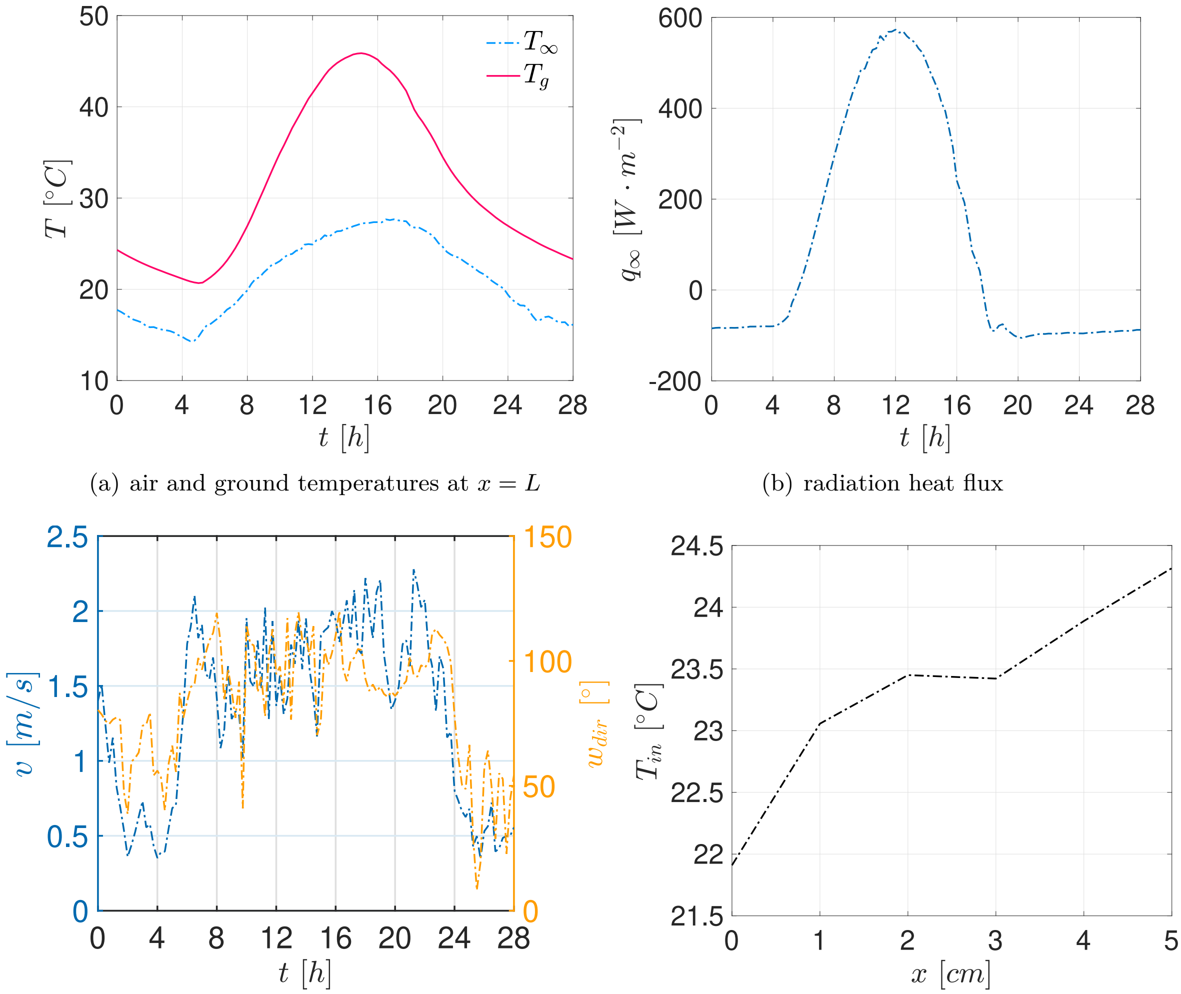


(a) air and ground temperatures at $x = L$

(b) radiation heat flux

(c) wind velocity and direction

(d) initial temperature

Figure 2. *Time variation of the air and ground temperatures* (a)*, radiation flux* (b)*, wind velocity and direction* (c) *and initial temperature* (d)*.*

vection and lienarized radiation were used for the analysis of the sensitivity coefficients at all times, by making $h_1 = h_2 = h_3 = 10$ W $\cdot$ m$^{-2}$ $\cdot$ K$^{-1}$ for $N_t = 3$ within $t \in [0, 6]$ h, $t \in [6, 24]$ h, and $t \in [24, 28]$ h time intervals, respectively (see Equation (5)) [41]. For the sensitivity coefficients analysis, the time variations of the air and ground temperatures at $x = L$, denoted by $T_\infty(t)$ and $T_g(t)$, respectively, shown in Figure 2(a), as well as $q_\infty(t)$, corresponding to the net radiation, presented in Figure 2(b), were used. Figures 3(a) - 3(e) present the time variations of the reduced sensitivity coefficients for $h_1$, $h_2$ and $h_3$, $C$ and $\kappa$, respectively. The reduced sensitivity coefficients with the largest magnitudes are those with respect to $\kappa$ and $h_2$, which also tend to be correlated. The other sensitivity coefficients attain maximum magnitudes about $0.7°C$ and are not linearly dependent, particularly because the sensitivity coefficients of $\{h_i\}_{i=1}^{i=3}$ are zero whenever these parameters are null. It is also interesting to note that the behaviors of the sensitivity coefficients are not affected by the sensor position, probably due to the small depth of ground considered. Therefore, all five sensors provide similar information for the solution of the inverse problem.

In order to further examine the correlation among the model parameters $(\kappa, C, h_1, h_2, h_3)$, the correlation matrix was calculated using the sensitivity coefficients presented in Figure 3:

$$\operatorname{corr}(\mathbf{P}) = \begin{array}{c} \\ \\ \\ \\ \\ \end{array}\begin{array}{ccccc} \kappa & C & h_1 & h_2 & h_3 \end{array}$$

$$\operatorname{corr}(\mathbf{P}) = \begin{array}{cc} & \begin{array}{ccccc} \quad\kappa\quad & \quad C\quad & \quad h_1\quad & \quad h_2\quad & \quad h_3\quad \end{array} \\ & \begin{pmatrix} 1 & -0.3292 & 0.6998 & -0.8907 & 0.6204 \\ -0.3292 & 1 & -0.1653 & 0.1233 & 0.1984 \\ 0.6998 & -0.1653 & 1 & -0.6366 & 0.4636 \\ -0.8907 & 0.1233 & -0.6366 & 1 & -0.6325 \\ 0.6204 & 0.1984 & 0.4636 & -0.6325 & 1 \end{pmatrix} \begin{array}{c} \kappa \\ C \\ h_1 \\ h_2 \\ h_3 \end{array} \end{array} \quad (18)$$

Similarly to the analysis of Figure 3, the correlation matrix indicates that the strongest linear dependence among the model parameters occurs between $\kappa$ and $h_2$, with the largest correlation coefficient of $-0.8907$. While classical techniques based only on the likelihood function would require that one of these two parameters be deterministically fixed for a successful solution of the inverse problem, the estimation of the model parameters within the Bayesian framework of statistics takes into account their prior information available, which are modeled in terms of probability distribution functions. In the Bayesian framework, the information provided by the likelihood function tends to reduce the original uncertainties of the parameters (modeled by their prior distributions) through the inverse analysis. In our study, for a successful estimation, Gaussian independent informative priors were provided for the thermal properties of the asphalt based on [40], with mean and standard deviation of: $2.1$ and $0.021$ $\mathsf{MJ \cdot m^{-3} \cdot K^{-1}}$, respectively, for C; and $2.23$ and $0.11$ $\mathsf{W \cdot m^{-1} \cdot K^{-1}}$, respectively, for $\kappa$. Therefore, the parameters that represent $h(t)$, with largest prior uncertainties and of most interest for the inverse analysis, are estimated here by appropriately taking into account uncertainties in all model parameters, instead of having some of them deterministically fixed.

### 4.3 Results of the parameter estimation problem

The Metropolis–Hastings algorithm was applied for solving the inverse problem. Results of the three case studies are presented in the next subsections.

In Cases A and B, the time varying heat transfer coefficient is approximated with only three parameters ($N_t = 3$) in Equation (5). In Case A, the surface heat transfer coefficients, $h_1$, $h_2$ and $h_3$, were defined for the time intervals between $t \in [0, 6]\,\mathsf{h}$, $t \in [6, 18]\,\mathsf{h}$, and $t \in [18, 28]\,\mathsf{h}$, respectively. These time intervals were chosen based on an analysis of Figure 2(b), when the net radiation flux have different magnitudes. In Case B, the time periods of $t \in [0, 6]\,\mathsf{h}$, $t \in [6, 24]\,\mathsf{h}$, and $t \in [24, 28]\,\mathsf{h}$ were chosen, based on the wind velocity presented in Figure 2(c), which shows different levels during these time intervals. In Cases A and B, independent Gaussian priors with a positive constraint were used for all parameters, with means and standard deviations presented in Table 2.

In Case C, the surface heat transfer coefficient was discretized as piece-wise constant values within each time interval when the measurements were taken (every 15 $\mathsf{min}$). Therefore, $N_t = 113$ in Equation (5). For this case, a Gaussian Markov Random Field prior was used for the parameter values representing the time variation of the surface heat transfer coefficient. The hyperprior for the parameter $\gamma$ in the Gaussian Markov Random Field prior was modeled as a Rayleigh distribution given by Equation (15), with $\gamma_0$ set as $2.22$ $\mathsf{m^4 \cdot K^2 \cdot W^{-2}}$. The same Gaussian priors of Case A were specified for the volumetric heat capacity and thermal conductivity.

The number of states required to reach equilibrium distributions in the Markov chains and the required computational time for the implementation of the Metropolis–Hastings algorithm for each case are presented by Table 1. Our codes were implemented in Matlab and run in a MacBook Air with a M1 processor and 8 Gbyte of RAM memory. This table shows that

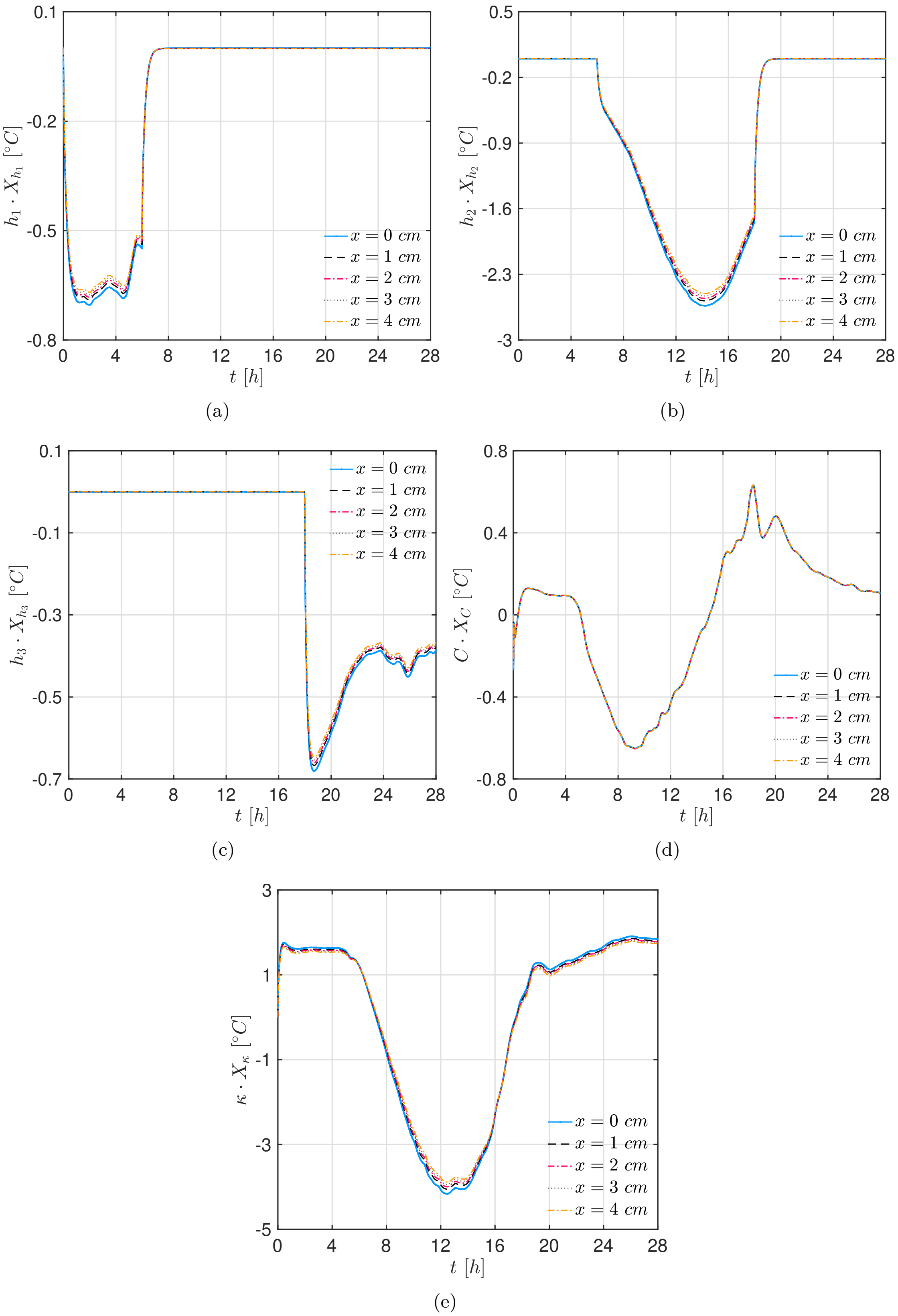


Figure 3. *Reduced sensitivity coefficients for each parameter:* $h_1$ *(a),* $h_2$ *(b),* $h_3$ *(c),* $C$ *(d),* $\kappa$ *(e).*

.

Cases A and B required smaller number of states to reach equilibrium distributions because of the smaller number of parameters than Case C.

Table 1. *Computational time required for each case.*

| Case | Number of states | CPU time |
|---|---|---|
| A | $2 \cdot 10^5$ | 23.5 **hours** |
| B | $2 \cdot 10^5$ | 23.5 **hours** |
| C | $10^6$ | 117 **hours** |

### 4.3.1 Cases A and B

Results of the estimation problem for Cases A and B are presented here. These cases are treated separately from Case C, since they involve only 3 parameters to represent the heat transfer coefficient ($N_t = 3$ in Equation (5)), with independent Gaussian priors presented in Table 2. This table also shows the means and standard deviations of the samples of the Markov chains after they reached equilibrium. Figures 4(a) - 4(d) present the Markov chains and the histograms after the burn-in period for $C$ and $\kappa$, respectively, in Cases A and B. Similar results are presented in Figures 5(a) - 5(d) for $h_1$, $h_2$ and $h_3$. These figures show that the Markov chains, simulated with 200 000 states, reached equilibrium distributions after about 50 000 states, so that the burn-in period was taken as 90 000 states. The histograms of the samples in the Markov chains after the burn-in period resemble Gaussian distributions. The values estimated for the parameters in Cases A and B were very close, with a relative differences between 5 and 7% for $h_1$, $h_2$, $h_3$, and 3% for $C$ and $\kappa$, respectively.

In order to test the robustness of the inversion procedure with $N_t = 3$ in Equation (5), Case A was repeated with different priors for $h_1$, $h_2$ and $h_3$, with means and standard deviations of 15 and 5 $\mathsf{W} \cdot \mathsf{m}^{-2} \cdot \mathsf{K}^{-1}$, respectively. The results obtained with this prior were identical to those presented in Table 2. Therefore, the inversion procedure was not affected by the mean values specified for the priors of the parameters representing the transient heat transfer coefficient. This was the case because of the large standard deviation of 5 $\mathsf{W} \cdot \mathsf{m}^{-2} \cdot \mathsf{K}^{-1}$ of both priors, which did not induce any bias on the estimated values. Moreover, the Gaussian priors specified for $C$ and $\kappa$ appropriately represented the original uncertainties in these parameters, which was reflected on the quite similar mean values estimated in both Cases A and B.

Table 2. *Statistics of the priors and of the marginal posteriors of the parameters for Cases A and B.*

| | | $h_1$ $[\mathsf{W} \cdot \mathsf{m}^{-2} \cdot \mathsf{K}^{-1}]$ | $h_2$ $[\mathsf{W} \cdot \mathsf{m}^{-2} \cdot \mathsf{K}^{-1}]$ | $h_3$ $[\mathsf{W} \cdot \mathsf{m}^{-2} \cdot \mathsf{K}^{-1}]$ | $C$ $[\mathsf{MJ} \cdot \mathsf{m}^{-3} \cdot \mathsf{K}^{-1}]$ | $\kappa$ $[\mathsf{W} \cdot \mathsf{m}^{-1} \cdot \mathsf{K}^{-1}]$ |
|---|---|---|---|---|---|---|
| Prior | mean | 10 | 10 | 10 | 2.10 | 2.27 |
| | std | 5 | 5 | 5 | 0.021 | 0.1135 |
| Case A | mean | 12.65 | 8.47 | 10.86 | 0.94 | 1.35 |
| | std | 0.02 | 0.01 | 0.01 | 0.0008 | 0.0008 |
| Case B | mean | 11.82 | 8.91 | 11.696 | 0.91 | 1.31 |
| | std | 0.02 | 0.0044 | 0.02 | 0.0009 | 0.0006 |

The acceptance rate of candidates generated with the proposal distribution in step 5 of the

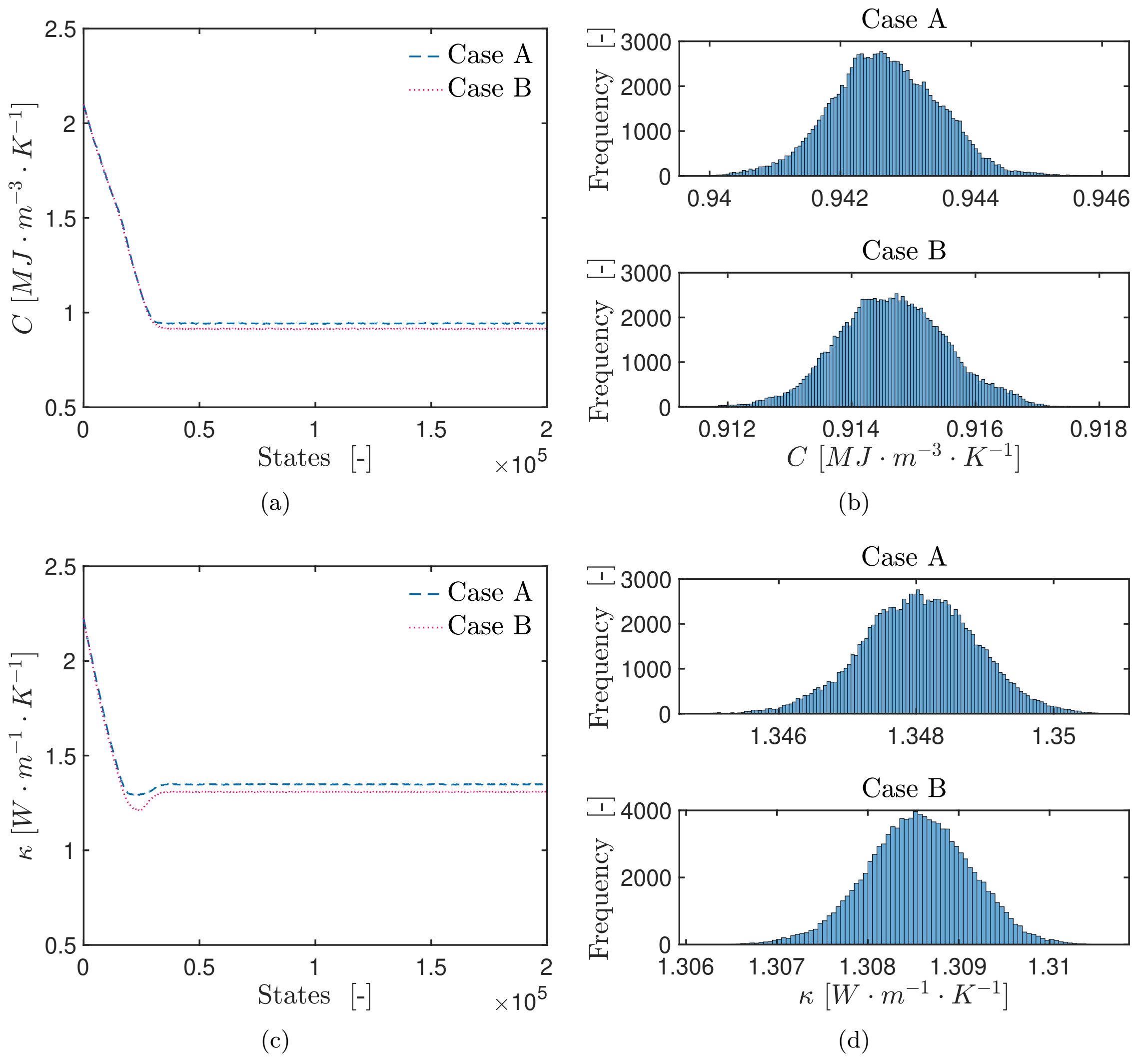


Figure 4. *Markov chains for:* $C$ (a) *and* $\kappa$ (c), *Histograms of the samples after the burn-in for:* $C$ (b) *and* $\kappa$ (d) *for both cases A and B.*

Metropolis–Hastings algorithm is presented in Figure 6(a). The acceptance rate was about 70% for Cases A an B. Figure 6(b) shows that the Markov chains of the posterior distributions, represented by $-\ln[\pi(P|Y)]$, decreased along the Markov chain. It can be seen that, after the burn-in period, which is indicated by the yellow vertical line, the Markov chains of the posterior distributions converged to equilibrium distributions in both cases.

Figure 7(a) presents the estimated heat transfer coefficients for Cases A and B, obtained as the means of the posterior distributions from the inverse problem solutions. The mean value of the prior distributions for the parameters representing the heat transfer coefficient *a priori* is also shown in this figure. As mentioned earlier, in Case A the total time was divided in three periods according to the net radiation flux variation. As it can be seen from Figure 7(a) and Figure 2(b), the lowest value of the net radiation flux variation corresponded to the largest value of the surface heat transfer coefficient. In case B, the total time was also divided in three periods, but in accordance with the wind velocity. Figure 7(a) and Figure 2(c) show that the surface heat transfer coefficient was inversely proportional to the wind velocity. This is contrary to the *empirical* law proposed in the literature [41]. Such behavior was probably due to the fact that wind and temperature measurements were carried out at different heights in the experiments.

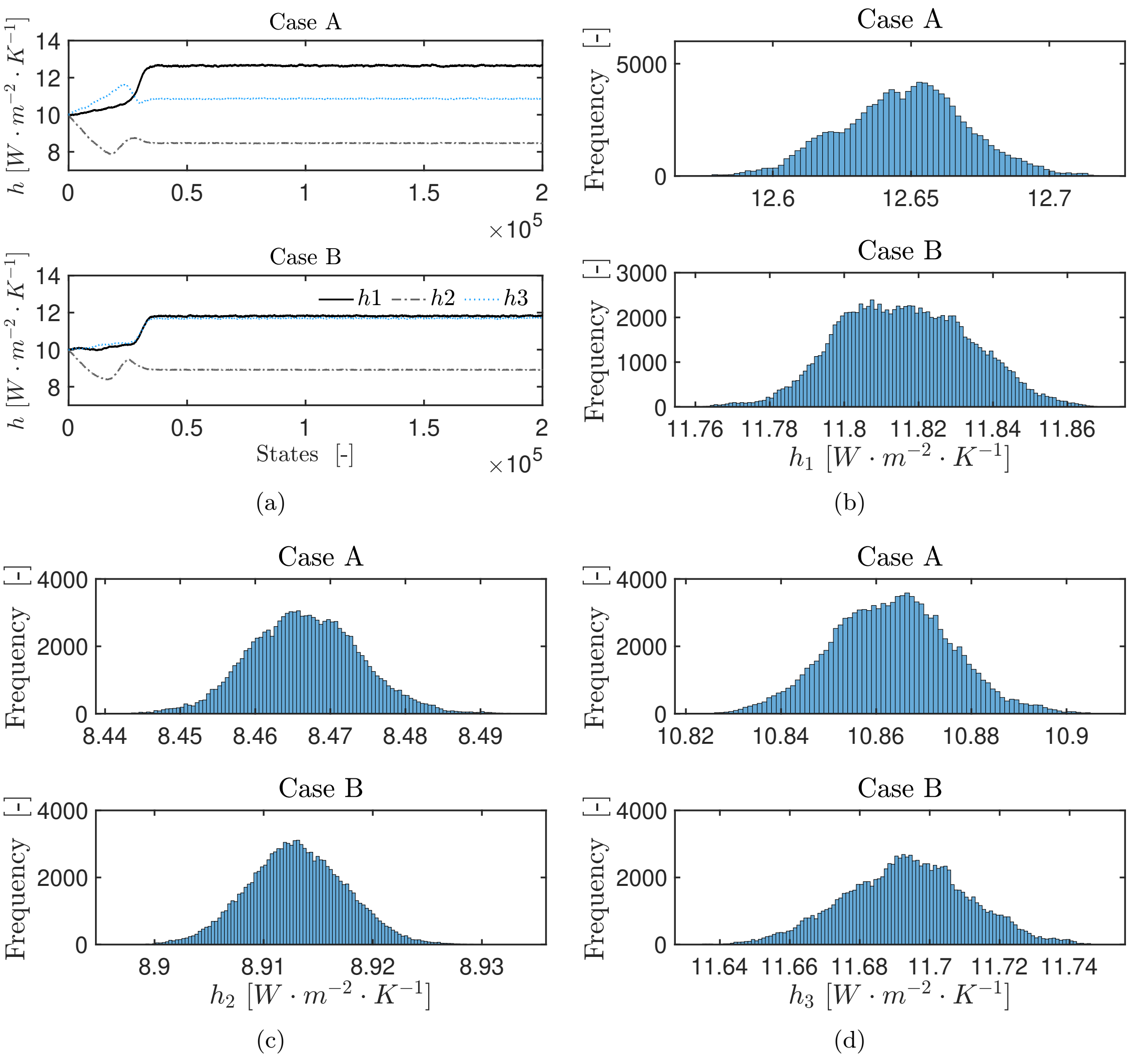


Figure 5. *Markov chains for:* $\{h_i\}_{i=1}^{i=3}$ (a)*. Histograms of the samples after the burn-in for:* $h_1$ (b)*,* $h_2$ (c)*, and* $h_3$ (d) *for both cases A and B.*

Furthermore, given the magnitude of the temperature difference between the ground surface and the ambient air during the experiment, natural convection effects may be more important than forced convection effects. Indeed, the magnitudes of the estimated heat transfer coefficients indicate mild cooling conditions, with values characteristic of natural convection coupled with linearized radiation in the longwave range. In general, Figure 7(a) shows that Cases A and B have quite similar behavior of the surface heat transfer coefficient.

After the estimation procedure, the direct problem was solved with the mean values of the marginal posterior distributions of thermal conductivity, volumetric heat capacity, and surface heat transfer coefficients, as well as with the prior mean values presented in Table 2. The corresponding temperatures computed at five measurement positions and the respective measurements are compared in Figures 7(b) - 7(f). In the figures showing the residuals, defined by the differences between measurements and predicted temperatures computed with estimated parameters, the grey areas show the standard deviation of the measurements around 0 °C. The measurement standard deviation, including also sensor location uncertanties, is 0.25 °C [26]. For both cases, residuals obtained with the mean parameters estimated with the solution of the inverse problems were lower than the residuals obtained with the original prior mean values, with

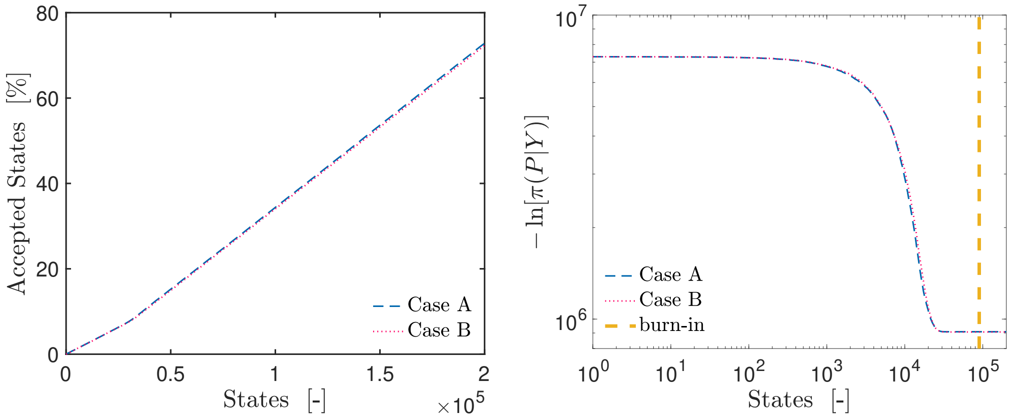


(a) (b)

Figure 6. *Acceptance rate* (a), *Variation of the posterior distribution* (b).

maximum relative discrepancies of 0.07%, 0.93%, 2.44%, 6.94% and 8.83% at $x = 0\,\mathsf{cm}$, $x = 1\,\mathsf{cm}$, $x = 2\,\mathsf{cm}$, $x = 3\,\mathsf{cm}$ and $x = 4\,\mathsf{cm}$, respectively. Note that the residuals were correlated and larger than the standard deviation of the measurements, thus indicating that the mathematical model with the parameters estimated in Cases A and B still demand further improvement for the representation of the experimental data. A more refined time discretization of the surface heat transfer coefficient is examined in the section below.

#### 4.3.2 Case C

This section presents the results of the inverse problem obtained with a Gaussian prior for $\kappa$ and $C$, and a Gaussian smoothness prior for the time varying surface coefficient $h(t)$. In this section, the estimated parameters $\kappa$ and $C$, obtained in Case A, are used as the Gaussian prior for $\kappa$ and $C$, respectively. While the surface heat transfer coefficient was discretized with $N_t = 3$ in Cases A and B above, piecewise constant values during time intervals coinciding with the available measurements, that is, every 15 $\mathsf{min}$, are utilized for Case C. Therefore, $N_t = 113$ in Equation (5), since the duration of the experiment is 28 $\mathsf{h}$. The present discretization of $h(t)$, with an unknown $h_i$ value for each time when measurements are available, corresponds to a function estimation approach for the solution of the inverse problem, which is regularized by the prior information considered for the unknown function. Nevertheless, the prior considered for $h(t)$ is improper, that is, with unlimited variance, and does not impose any constraints on the estimated function, except for smoothness [34].

Figure 8(a) shows that the acceptance rate for Case C was similar to those for Cases A and B, that is, around 70%. The evolution of the posterior according to the number of states is given in Figure 8(b). This figure shows that the chain converged to an equilibrium distribution after about $3{\cdot}10^{5}$ states. Figures 9(a) - 9(d) present the Markov chains for the parameters $C$, $\kappa$ and $h$ (at selected times), respectively. As for Figure 8(b), these figures show that the Markov chains, simulated with $10^{6}$ states, reached equilibrium after about $3 \cdot 10^{5}$ states. Consequently, such value was taken as the burn-in period. Figure 10 presents the normalized autocovariance function of the posterior, with the corresponding integrated autocorrelation time (IACT) estimated as 11402. As expected, the normalized autocovariance function of the posterior tended to zero, and then became influenced by noise. However, we note that IACT was high, because of the large acceptance rate shown by Figure 8(a).

The histograms of the samples of the Markov chains are presented in Figures 11(a) - 11(f), for $C$, $\kappa$ and $h$ at selected times, respectively. From Figures 11(a) and 11(f), the posterior

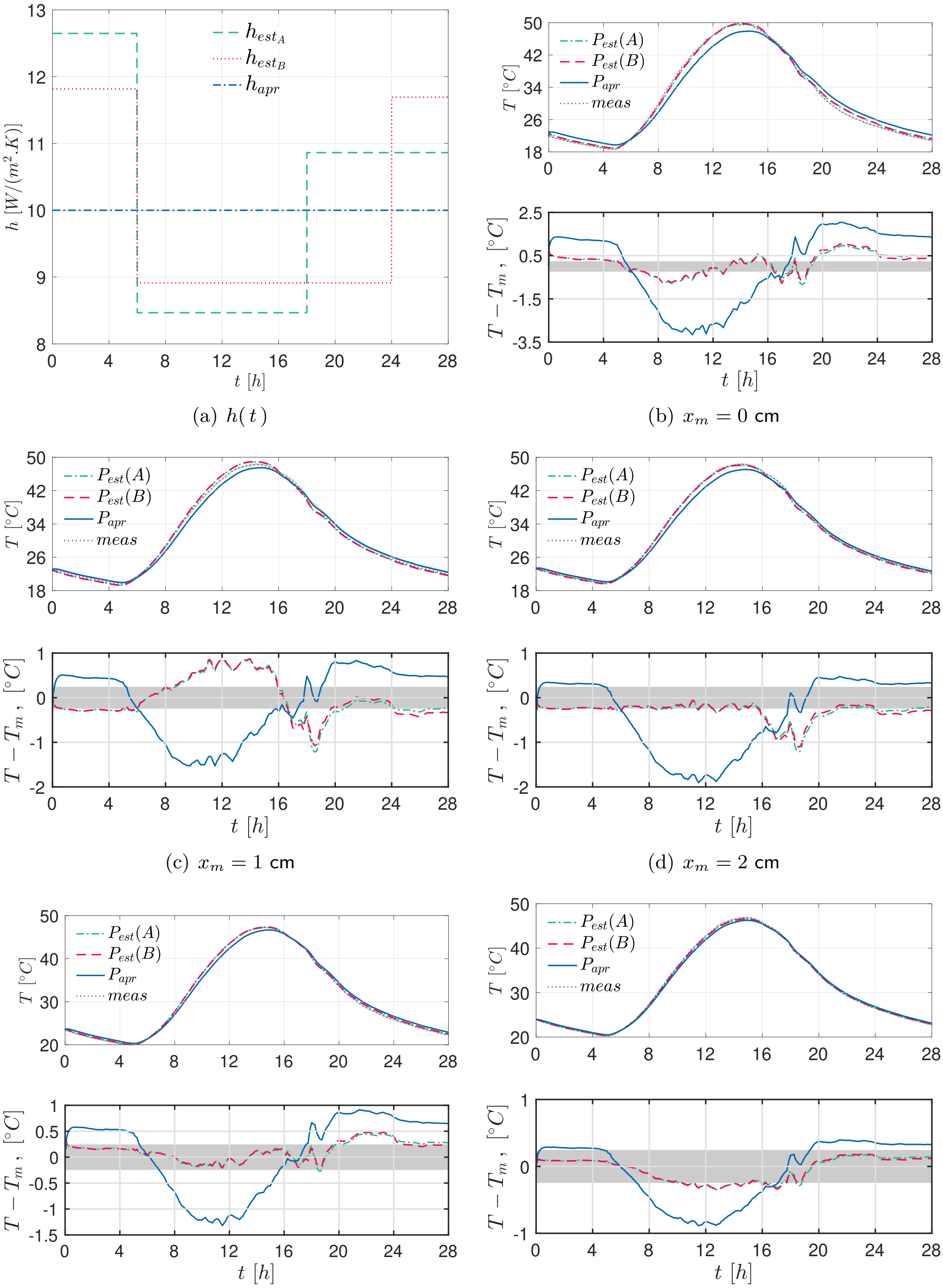


(a) $h(t)$ (b) $x_m = 0$ cm

(c) $x_m = 1$ cm (d) $x_m = 2$ cm

(e) $x_m = 3$ cm (f) $x_m = 4$ cm

Figure 7. *Time varying surface heat transfer coefficient* (a). *Computed temperatures with mean of the estimations and literature values, and measured values of temperature at several sensor locations* (b) - (f). *The grey shaded area represents the measurement uncertainty.*

distributions of the estimated quantities resembled GAUSSIAN distributions. Regarding the surface heat transfer coefficient, the marginal posteriors exhibited coefficients of variations smaller than 1 %. Those results are consistent with the analysis of the relative differences of means of the estimated heat transfer coefficients obtained with GEWEKE's analysis [42], as illustrated in Figure 12(a). The relative difference of the means was computed with the first 10 % and the

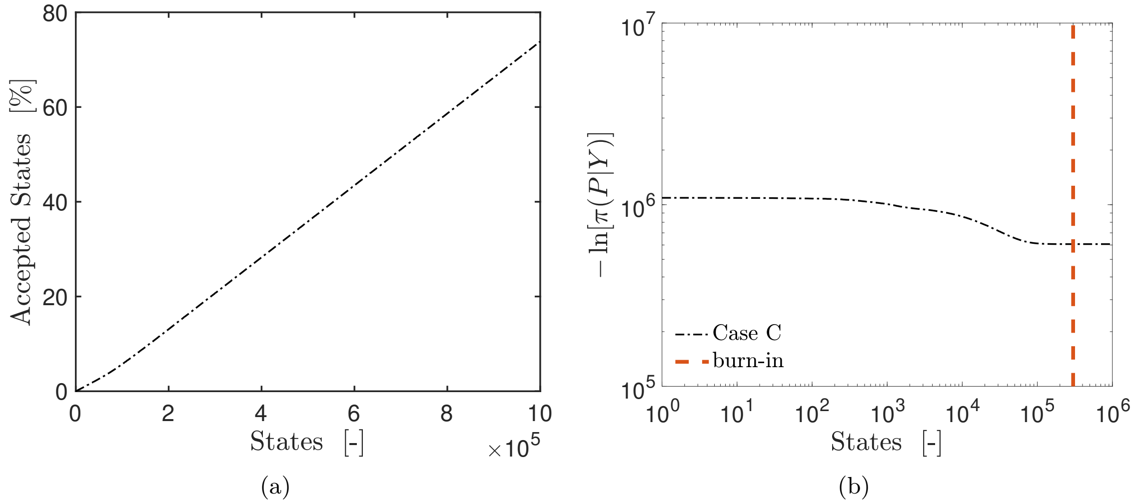


Figure 8. *Number of accepted candidates* (a) *and variation of the posterior distribution* (b) *according to the number of states.*

last 50 % of samples of the MARKOV chains after reaching equilibrium for each parameter [42]. The relative difference of means were larger for times between 1 and 7 h, as well as between 17 and 28 h. However, these differences are less than $10^{-3}$. The box plots of the samples at the beginning and end of the converged MARKOV chains are also shown by Figures 12(b) - 12(d), for times $t = 7$ h, 14 h and 21 h, respectively. Figures 12(b) - 12(d) show quite similar distributions at the beginning and end of the MARKOV chains. Figures 12(a) - 12(d) show that the MARKOV chains reached equilibrium distributions with the burn-in period of 300 000 states considered for Case C.

The mean and standard deviation values of each unknown parameters, calculated after the burn-in period are presented in Table 3.

Table 3. *Statistics for the marginal posterior distributions of the parameters.*

| parameters | | $h(t)$ | | | | | $C$ | $\kappa$ |
|---|---|---|---|---|---|---|---|---|
| unit | | $\left[\mathrm{W \cdot m^{-2} \cdot K^{-1}}\right]$ | | | | | $\left[\mathrm{MJ \cdot m^{-3} \cdot K^{-1}}\right]$ | $\left[\mathrm{W \cdot m^{-1} \cdot K^{-1}}\right]$ |
| time instant | | $t = 0\,h$ | $t = 7\,h$ | $t = 14\,h$ | $t = 21\,h$ | $t = 28\,h$ | – | – |
| estimated | mean | 16 .67 | 6 .43 | 10 .29 | 14 .33 | 12 .92 | 0 .99 | 1 .31 |
| | std | 0 .09 | 0 .06 | 0 .02 | 0 .08 | 0 .13 | 0 .0008 | 0 .0007 |

Figure 13(a) presents the surface heat transfer coefficients estimated with Cases A, B and C. The grey area for Case C is given by two times the standard deviations around the means of the estimated samples of the MARKOV chains. The behavior of the surface heat transfer coefficients of all cases were similar and consistent, despite the different time discretizations that were used. Figure 13(b) shows the surface heat transfer coefficient estimated with Case C and the measured wind velocity. For the time periods $t \in [0, 6]$ h and $t \in [21, 28]$ h the heat transfer coefficient decreased with the velocity. For the period $t \in [6, 21]$ h, the relation between both quantities was less obvious and can be explained by several reasons, such as: the velocity exhibited fluctuations with high frequency and at different wind orientations as illustrated in Figure 2(c); the temperature and wind velocity measurements were carried out at

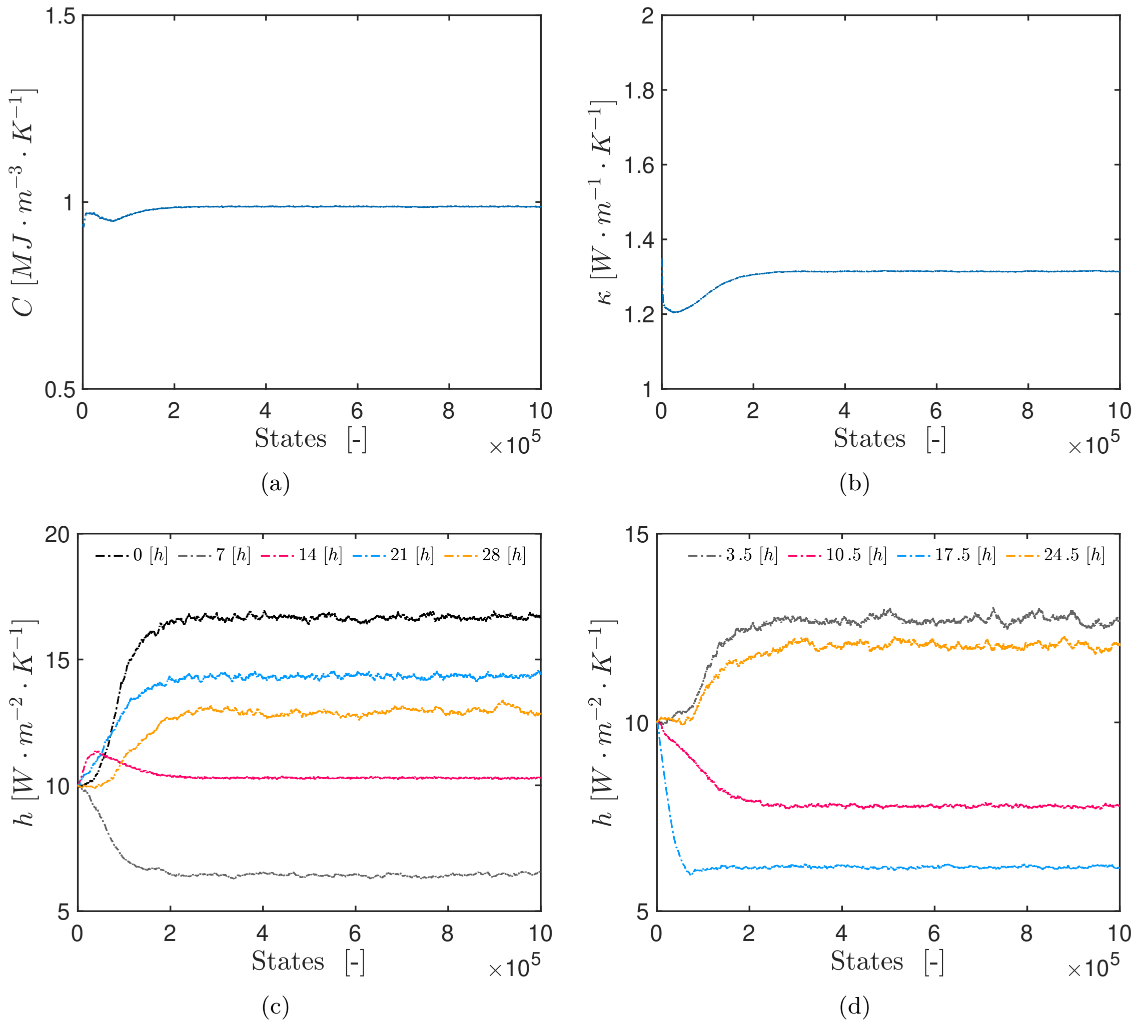


Figure 9. *Markov chains for* $C$ (a), $\kappa$ (b) *and for various surface heat transfer coefficients* (c) - (d).

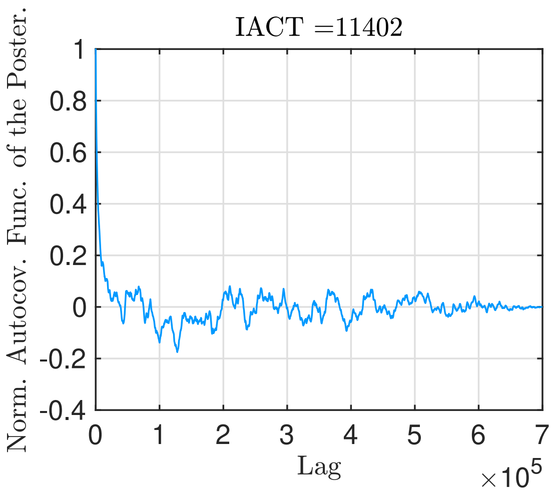


Figure 10. *Variation of the normalized autocovariance function of the posterior.*

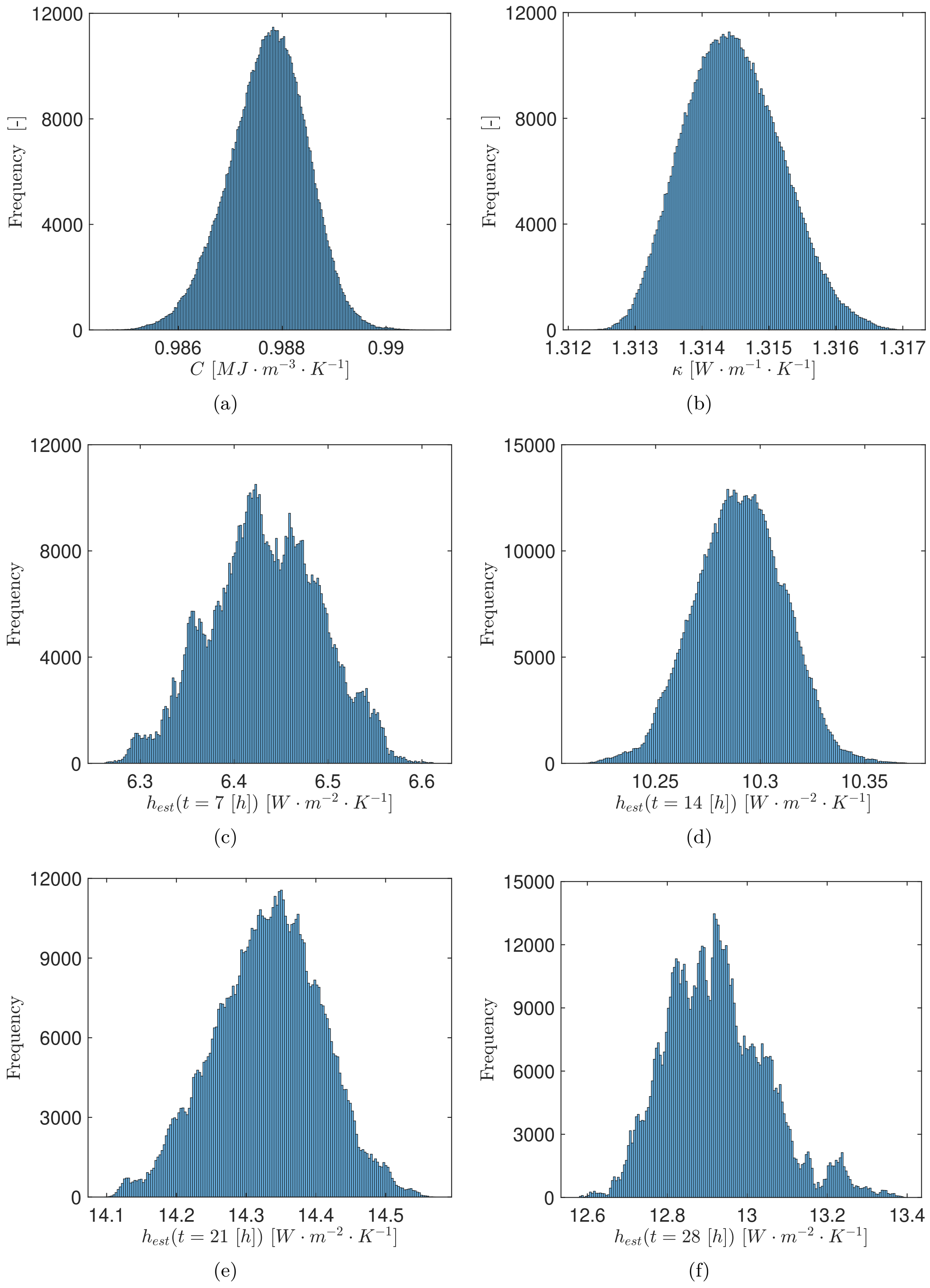


Figure 11. *Histograms of the samples after the burn-in period for* $C$ (a), *for* $\kappa$ (b) *and for* $h$ *at* $t = 7\,h$ (c), $t = 14\,h$ (d), $t = 21\,h$ (e), *and* $t = 28\,h$ (f).

different heights [29], not necessarily outside the thermal and velocity boundary layers over the surface of the ground; and natural convection effects. Figure 13(a) shows that around $t = 18$ h

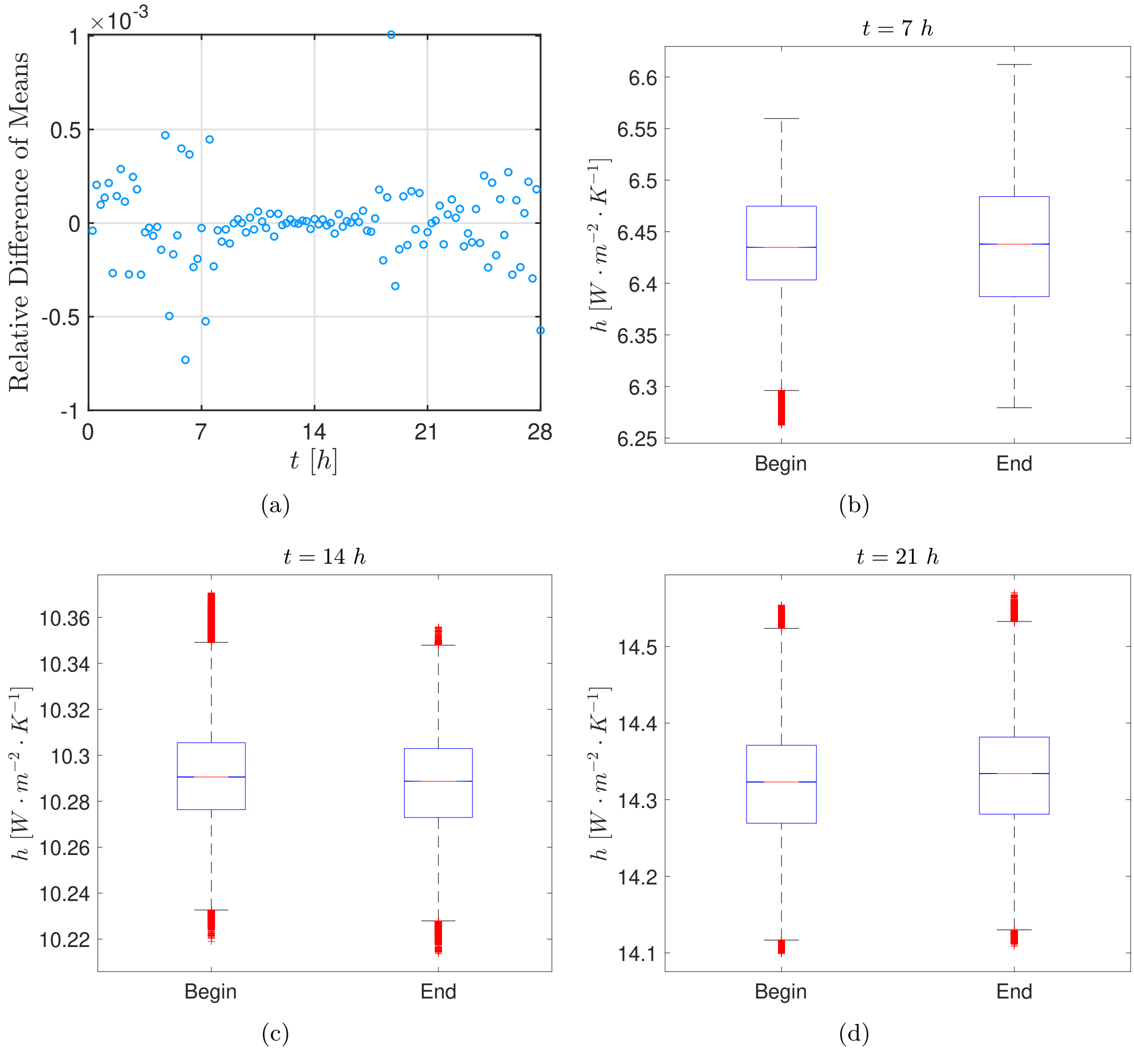


Figure 12. *Relative difference of means of the estimated surface heat transfer coefficients at each observation time* (a). *Range of the mean values of the surface heat transfer coefficient at* $t = 7[\mathrm{h}]$ (b), $t = 14[\mathrm{h}]$ (c) *and* $t = 21[\mathrm{h}]$ (d) *between begin and last part of the Markov chain.*

the surface heat transfer coefficient oscillated. It was examined if such oscillations were due to the ill-posed character of the inverse problem. Therefore, the inverse problem was solved for several *a priori* values of the hyperparameter $\gamma_0 \in \{2.22\,,\,3.33\,,\,22.22\ \mathrm{m}^4 \cdot \mathrm{K}^2 \cdot \mathrm{W}^{-2}\}$. The results obtained with these different values of $\gamma_0$ where identical, as shown by the superposed curves of estimated h(t) mean values in Figure 13(b).

After the estimation procedure, the direct problem was computed with the mean values of the posterior distributions of each parameter, as well as with the prior mean and literature values of the parameters. The corresponding temperatures computed at five measurement positions and the respective measurements are compared in Figures 14(a)-14(e). The residuals are also presented in these figures. Temperatures computed with the estimated values were in better agreement with the measurements than the ones computed with the prior/literature values of the parameters. Moreover, residuals for Case C were smaller than those for Cases A and B (see also Figures 7(b) - 7(f)). The agreement between estimated and measured temperatures was improved by at least 8 % with the time discretization of the surface heat transfer coefficient used in Case C, as compared to Cases A and B. Therefore, the function estimation approach of Case C was more appropriate to represent the actual physical behavior of the problem under analysis,

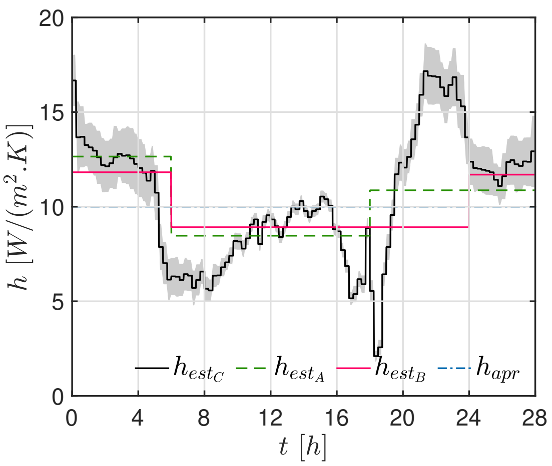


(a) $h(t)$

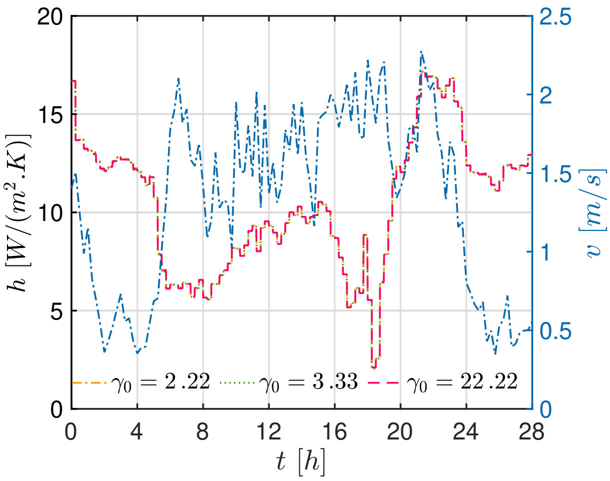


(b) $h(t)$ and $v(t)$

Figure 13. *Time varying surface heat transfer coefficient, the grey shaded area represents two standard deviations around the mean values presented* (a).*Time varying surface heat transfer coefficient with different values of* $\gamma_0$ *and wind velocity* (b).

than the coarse time discretization applied for $h(t)$ in Cases A and B. Despite being small, the residuals for all cases (see Figures 7(b) - 7(f), 14(a)-14(e)) exhibit some type of signature, demonstrating that improvements on the mathematical model would still be required to cope with other phenomena not reported during the experiments, which could be accounted for in the formulation of the direct problem. Such phenomena are most likely of random nature, like clouds affecting the solar irradiation or physical barriers (large vehicles, for example) disturbing the velocity and thermal boundary layers. The normalized autocovariance functions of the residuals at each measurement location were computed for each of the cases examined in this work. An analysis of the normalized autocovariance functions presented by Figure 15 reveal that the correlations of the residuals were not significantly affected by the time discretization used for h(t), that is, cases A, B and C, and should be caused by other phenomena.

Effects of the computed convective and measured radiative heat fluxes were also examined. These fluxes are presented in Figure 16. This figure also presents the temperature difference $T_\infty(t) - T(x=0,t)$ given by the black line. At about 18 h, the radiative heat flux decreased and became negative due to the decrease in the solar irradiation. Meanwhile, during the whole experiment the convective flux was negative, since the ground surface was warmer than the ambient air. As a result of the energy balance at the ground surface, the temperature increased from 6 to 14 h, and then it decreased afterwards as shown by Figure 14(a). The instability on the surface heat transfer coefficient observed in Figure 13(a) can be due to the radiative heat flux that changed sign at 18 h, which might have affected the estimation procedure. In order to examine the effect of the sudden variation of the radiative flux on the estimated heat transfer coefficient observed at $t = 18$ h in Figure 16, the inverse problem was also solved with a smoothed radiative flux using a moving average filter of 1.5 h. However, the obtained results were identical to those presented in Figure 13(a), which were directly obtained with the raw measured data without filtering. Therefore, the estimation of the surface heat transfer coefficient was performed with success and led to a better agreement between the model predictions and the measured temperatures.

In addition to these investigations, the influence of using different numbers of sensors was examined. The sensitivity analysis in Figure 3 shows that the sensitivity functions are very similar for different sensor positions. Therefore, using five sensors in the inverse problem does not provide significantly more information. For Case C, which involves the simultaneous estimation of $h(t)$, $C$, and $\kappa$, the problem involves $N_t + 2$ unknown parameters, where $N_t$ is the number of measurement according to time. Therefore, the measurement of at least two sensors are needed to solve the inverse problem for Case C. The inverse problem was solved using only two sensors

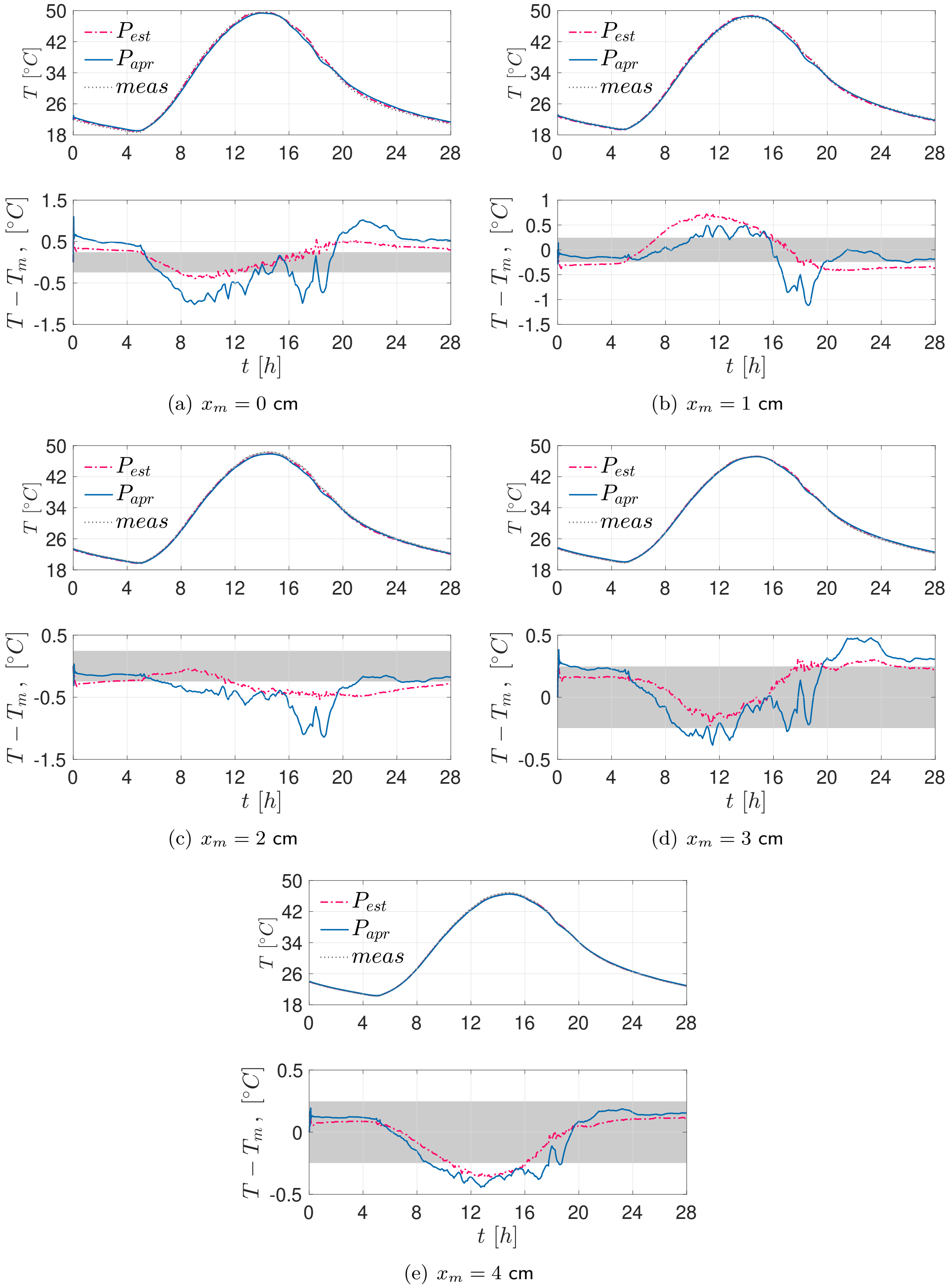


(a) $x_m = 0$ cm

(b) $x_m = 1$ cm

(c) $x_m = 2$ cm

(d) $x_m = 3$ cm

(e) $x_m = 4$ cm

Figure 14. *Computed temperatures with mean of the estimations and literature values, and measured values of temperature at several sensor locations* (a) - (e). *The grey shaded area represents the measurement uncertainty.*

located at $x = 0$ and $x = 1\,\mathrm{cm}$ for case C. Results presented in Figure 17 indicate that the estimations obtained using 2 and 5 sensors are similar. Therefore, it can be concluded that a

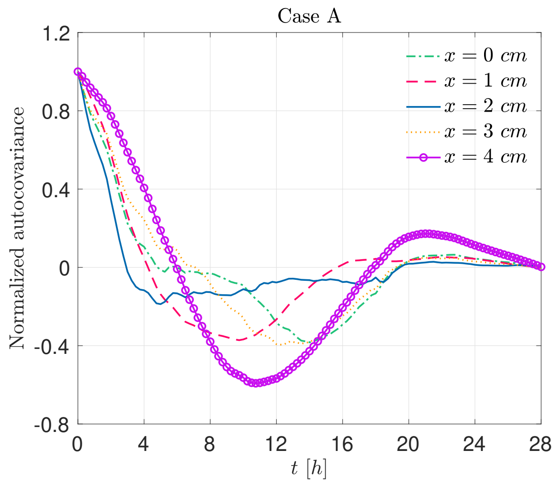


(a)

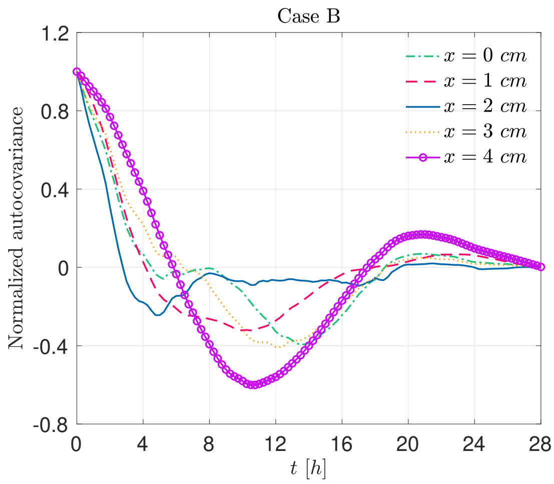


(b)

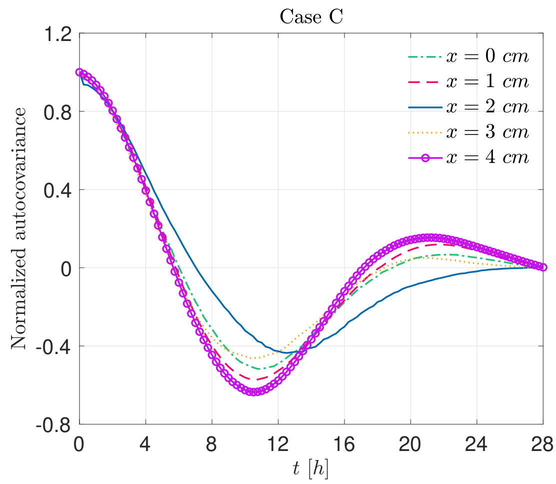


(c)

Figure 15. *Normalized autocovariances of the residulas for: Case A (a); Case B (b); Case C (c).*

reduced number of sensors is sufficient to reliably solve the current inverse problem.

# 5 Influence of the surface heat transfer coefficient on the energy balance in a urban scene

The previous section dealt with the estimation of the time varying heat transfer coefficient at the ground surface, as well as of the ground thermophysical properties. In the context of better assessing the energy balance of the radiation flux in the urban environment, a simulation was performed with a micro-climatic simulation tool [43]. The physical problem considers: (i) outside short-wave radiative heat balance, (ii) outside long-wave radiative heat flux for the whole urban scene and the sky, (iii) 1D conduction through all the elementary surface of the urban scene (ground, walls, roofs, etc), (iv) inside building zone long-wave radiative heat fluxes and air temperature calculation. For the ground, the physical problem solves the equations presented before (Equations (1) - 4). The time step was set to 15 min with 8 days of simulation.

The geometric configuration represents a real urban environment, inspired from the experi-

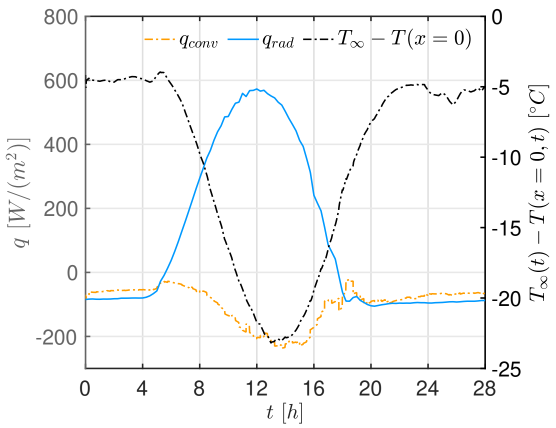


Figure 16. *Time varying heat fluxes at the surface of the ground and temperature difference* $T_\infty(t) - T(x=0,t)$.

mental platform [44]. A schematic illustration of the case study is presented in Figure 18. The platform was composed of 9 empty concrete tanks arranged in three rows, representing a reduced version of buildings and streets. The streets were set with a ratio building height / street width of 1.1 and oriented North-South. Further details on the geometrical configurations can be obtained in [44]. The tanks were composed of concrete walls of 4 cm with thermal properties: $\kappa = 2.4 \, \mathsf{W} \cdot \mathsf{m}^{-1} \cdot \mathsf{K}^{-1}$ and $C = 1.9 \, \mathsf{MJ} \cdot \mathsf{m}^{-3} \cdot \mathsf{K}^{-1}$ [44]. For the first 5 cm, the thermophysical properties of the ground were those estimated in Case C and reported in Table 3. For the deeper layers, the thermal properties were the ones considered in [8]. The measured temperature at $z = 75$ cm was used as boundary condition in the ground. The solar reflectivity was 0.64 for the wall and 0.36 for the ground [8]. The short-wave radiation flux was decomposed as direct and diffuse components calculated using the global component measured during the experimental campaign (see Section 4.1) with the method described in [45]. The outside temperature was directly given from the experimental data. Last, the long-wave radiation flux was computed from the measurement of incoming long-wave (thermal infrared) radiation.

Two simulations were performed considering the whole long-wave radiation balance between the surfaces and the heat conduction through the ground and walls for the whole urban scene. Results are presented for two zones of interest highlighted in red in Figure 18. The first simulation corresponds to standard simulation: the ground surface heat transfer coefficient was computed using the wind air velocity and the following empirical correlations [46]:

$$h(v) = 4 + 4 \cdot v \, .$$

In most of the standard simulations at district or building scales, to save computational effort with CFD simulations, the wind velocity was taken from the nearest airport meteorological station. In this case, it corresponds to the Nantes-Atlantique airport (around 10 km distant from the case study site), obtained from [47] for the exact day of the investigations (June $6^{th}$, 2004). The second simulation was carried out using the time varying ground surface heat transfer coefficient estimated in case C of this work ($h_{est_C}(t)$). The coefficients considered for the two simulations are presented in Figure 19(a). Figure 19(b) shows the surface temperature of the whole urban environment computed with the heat transfer coefficient given by $h_{est_C}(t)$. The temperature was lower in the urban canyon due to the shading effects. The difference between the two simulations are given in Figures 19(c)–19(f). The zones of interest for the analysis of the thermal balance are highlighted in red in Figure 18 (and black in Figure 19(b)), corresponding to the surface ground in the canyon and a wall of a close building. A difference of more than 2 °C was observed on the surface ground temperature. The difference was lower for the surface building wall temperature with a magnitude of 0.1 °C around noon. Regarding the received

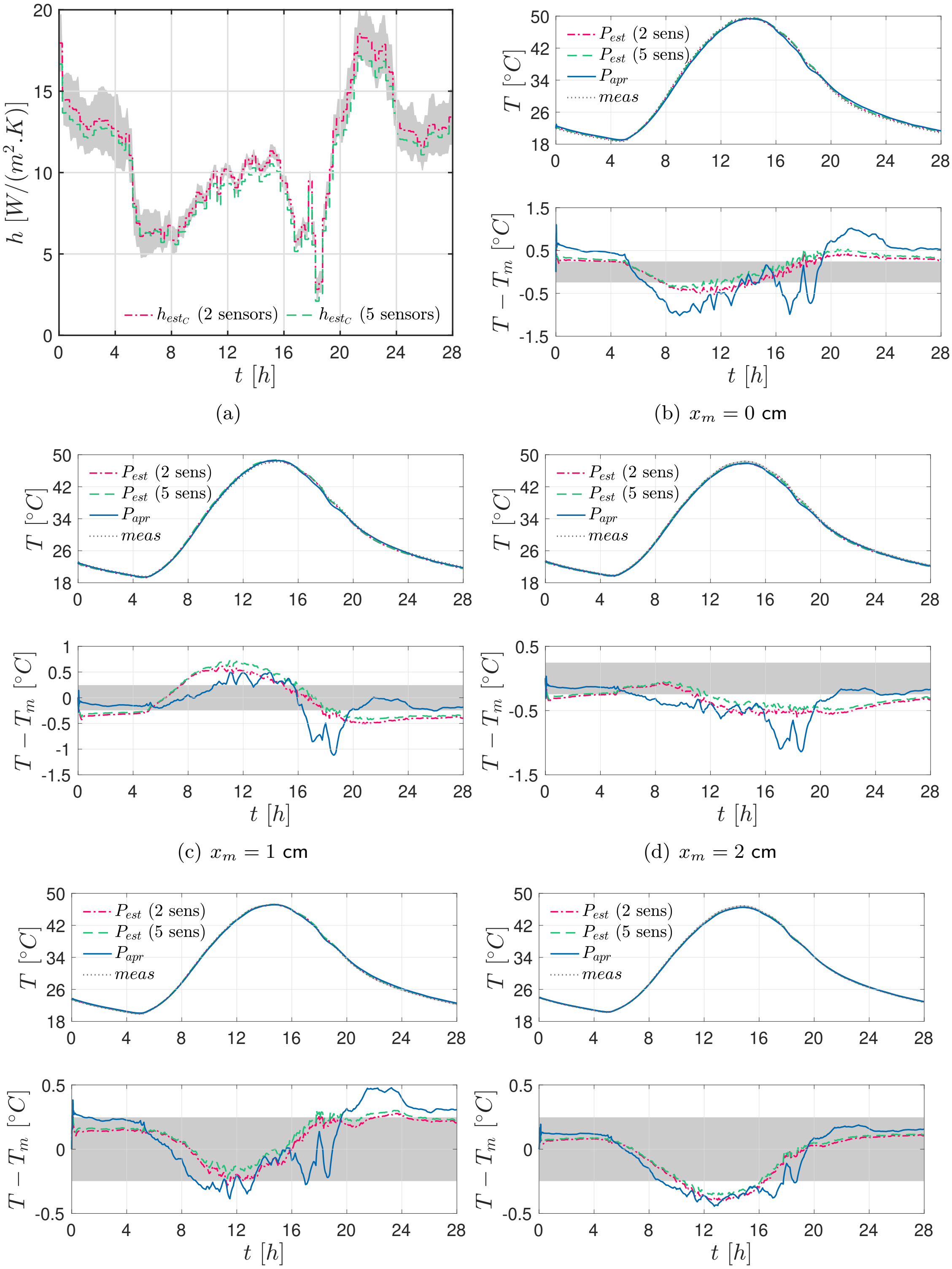


(a) (b) $x_m = 0$ cm

(c) $x_m = 1$ cm (d) $x_m = 2$ cm

(e) $x_m = 3$ cm (f) $x_m = 4$ cm

Figure 17. *Time varying surface heat transfer coefficient* (a). *Computed temperatures with mean of the estimations (obtained from* 2 *and* 5 *sensors)and literature values, and measured values of temperature at several sensor locations* (b) - (f). *The grey shaded area represents the measurement uncertainty.*

long-wave radiation flux $q_{LW}$ $\left[\mathsf{W}\cdot\mathsf{m}^{-2}\right]$ illustrated in Figures 19(e)-19(f), it increased during the day with the increase of the surface temperature of the urban scene. The difference between the two simulations reached almost 15 $\mathsf{W}\cdot\mathsf{m}^{-2}$ and 4 $\mathsf{W}\cdot\mathsf{m}^{-2}$ for the ground and building wall, respectively. This analysis highlights the requirement of accurately modeling the surface heat transfer coefficient for reliable assessment of the energy balance at the urban scale.

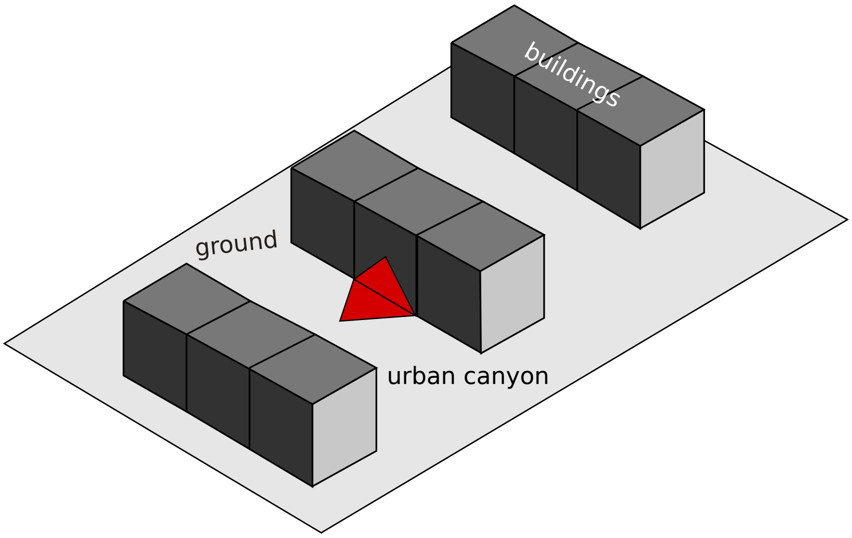


Figure 18. *Illustration of the urban scene with the zone of interests highlighted in red.*

## 6 Conclusion

In this work, an inverse one-dimensional heat conduction problem was solved to estimate the unknown thermal conductivity, volumetric heat capacity and time varying surface heat transfer coefficient. The Bayesian framework with the MCMC algorithm was used to explore the posterior distributions of the unknown parameters based on their prior distributions and on the likelihood function that models the measurement errors. The measured temperatures were obtained from an experimental campaign with *in-situ* monitoring of ground with 5 sensors. Three approximations were considered for the time varying surface heat transfer coefficients. For the first two case studies, A and B, the coefficient was defined as piecewise constant for three time periods. Gaussian priors were applied for the unknown parameters. Retrieved parameters led to a lower residual of the temperature, as compared to direct computations using parameters from the literature. The third case studied, case C, a value of the surface heat transfer coefficient was estimated for each time interval when measurements were available (every 15 min). For this parameter, a Gaussian smoothness prior was considered. Results show more accurate predictions of the calibrated model with the heat transfer coefficient estimated in Case C, than in cases A and B.

A comparison at the urban scale was also performed between a standard simulation, which assumed a ground surface coefficient computed with the wind velocity measured at the nearest airport meteorological station, and a simulation using the estimated time varying coefficient from case C. The results obtained in this work highlight the importance of accurate modeling the heat transfer coefficient for reliable assessment of the energy balance of the urban environment. This work can have direct implications for urban design and policy. Improved knowledge of ground thermal properties and more accurate estimation of time-varying surface heat transfer coefficients can enhance the reliability of urban microclimate models. Those models are used to assess heat stress, and climate adaptation strategies. In particular, better representation of heat

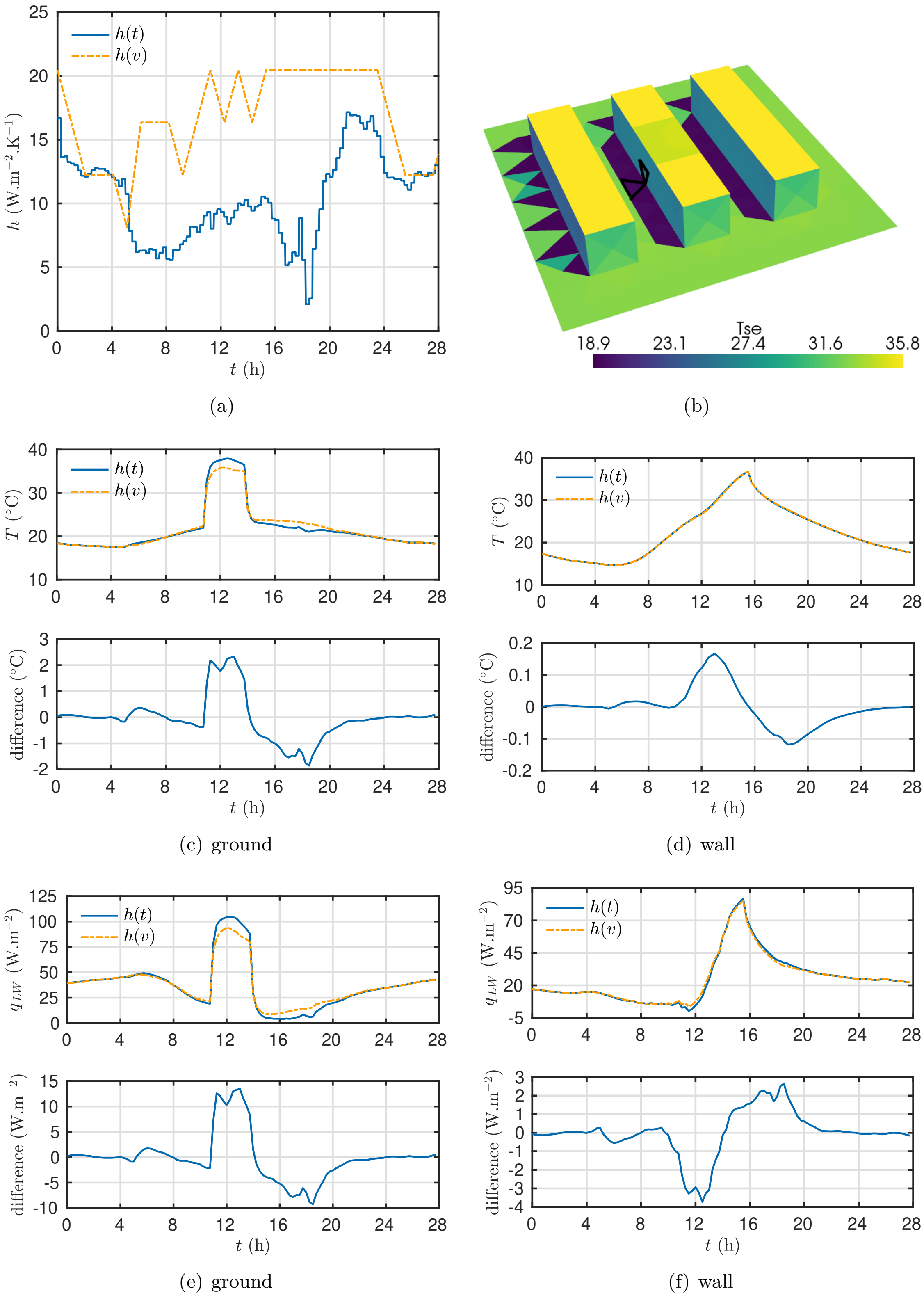

Figure 19. *Time varying ground surface coefficient* (a) *for the urban environment simulation. Computed surface temperature at* $t = 10.75$ h *for the case* $h(t)$ (b). *Time varying surface temperature and long wave radiation flux for the ground* (c,e) *and the building wall* (d,f).

transfer at the ground–atmosphere interface can inform pavement material selection and design, allowing engineers to optimize surface layers for thermal comfort. The refined parameterizations developed here also enable more realistic simulations of passive cooling strategies, such as vegetalization, pavement watering or the use of reflective surfaces. At the policy level, these advances provide municipalities with a stronger scientific basis for evidence-based interventions aimed at mitigating urban heat islands, improving outdoor comfort, and supporting sustainable urban development.

# Nomenclature

| | | |
|---|---|---|
| | *Latin letters* | |
| $C$ | volumetric heat capacity | $[\mathsf{J} \cdot \mathsf{m}^{-3} \cdot \mathsf{K}^{-1})]$ |
| $c_p$ | specific heat | $[\mathsf{J} \cdot \mathsf{kg}^{-1} \cdot \mathsf{K}^{-1})]$ |
| $L$ | ground depth | [m] |
| $t_f$ | final time | [s] |
| $T$ | temperature | [K] |
| $T_\infty$ | temperature of the air | [K] |
| $T_g$ | temperature of the ground | [K] |
| $T_{in}$ | initial temperature | [K] |
| $h$ | surface heat transfer coefficient | $[\mathsf{W} \cdot \mathsf{m}^{-2} \cdot \mathsf{K}^{-1}]$ |
| $q_\infty$ , $q_{LW}$ | radiation flux | $[\mathsf{W} \cdot \mathsf{m}^{-2}]$ |
| $t$ | time | [s] |
| $x$ | spatial coordinate | [m] |
| $U$ | dimensionless temperature | $[-]$ |
| $k$ | dimensionless heat conductivity | $[-]$ |
| $Fo$ | Fourier number | $[-]$ |
| $Bi^L$ | Biot number | $[-]$ |

| | | |
|---|---|---|
| | *Greek letters* | |
| $\kappa$ | thermal conductivity | $[\mathsf{W} \cdot \mathsf{m}^{-1} \cdot \mathsf{K}^{-1}]$ |
| $\alpha$ | thermal diffusivity | $[\mathsf{m}^{2} \cdot \mathsf{s}^{-1}]$ |
| $\rho$ | density | $[\mathsf{kg} \cdot \mathsf{m}^{-3}]$ |

| | |
|---|---|
| | *Subscripts and superscripts* |
| $*$ | dimensionless parameter |
| $apr$ | *a priori* parameter value |
| $est$ | estimated parameter value |

# Acknowledgments

This research is funded by the Committee of Science of the Ministry of Science and Higher Education of the Republic of Kazakhstan (Grant No.AP32318683). The authors acknowledge DSG 2021 and the French National Research Agency (ANR) as part of the “JCJC CE-22 AAPG 2023” program (project TOPS) for the financial support.

# References

[1] A review on reflective materials for cementitious composites. *Journal of Building Engineering*, 101:111877, 2025. 1

[2] Abbas Mohajerani, Jason Bakaric, and Tristan Jeffrey-Bailey. The urban heat island effect, its causes, and mitigation, with reference to the thermal properties of asphalt concrete. *Journal of Environmental Management*, 197:522–538, 2017. 1

[3] C. Maduabuchukwu Nwakaire, C. Chuen Onn, S. Poh Yap, C. Wah Yuen, and P. Dinwoke Onodagu. Urban heat island studies with emphasis on urban pavements: A review. *Sustainable Cities and Society*, 63:102476, 2020. 1

[4] M. H. Azam, J. Bernard, B. Morille, M. Musy, and H. Andrieu. A pavement-watering thermal model for solene-microclimat: Development and evaluation. *Urban Climate*, 25:22–36, 2018. 1

[5] M. Musy, L. Malys, B. Morille, and C. Inard. The use of solene-microclimat model to assess adaptation strategies at the district scale. *Urban Climate*, 14:213–223, 2015. Cooling Heat Islands.

[6] Feifei Dong and Takashi Asawa. A simulation study on building-scale strategies for urban heat island mitigation and building energy consumption: Case study in japan. *Building and Environment*, 268:112311, 2025.

[7] Eduardo-Javier Elizondo-Martínez, Valerio-Carlos Andrés-Valeri, Daniel Jato-Espino, and Jorge Rodriguez-Hernandez. Review of porous concrete as multifunctional and sustainable pavement. *Journal of Building Engineering*, 27:100967, 2020. 1

[8] M.H. Azam, B. Morille, J. Bernard, M. Musy, and R. Fabrice. A new urban soil model for solene-microclimat: Review, sensitivity analysis and validation on a car park. *Urban Climate*, 24:728–746, 2018. 1, 22

[9] M. Colombert, Y. Diab, J.L. Salagnac, and D. Morand. Sensitivity study of the energy balance to urban characteristics. *Sustainable Cities and Society*, 1(3):125–134, 2011.

[10] S.W. Rees, Z. Zhou, and H.R. Thomas. Ground heat transfer: A numerical simulation of a full-scale experiment. *Building and Environment*, 42(3):1478–1488, 2007. 1

[11] G. Hu, L. Zhao, X. Wu, R. Li, T. Wu, C. Xie, Y. Qiao, and G. Cheng. Comparison of different soil temperature algorithms in permafrost regions of qinghai-xizang (tibet) plateau of china. *Cold Regions Science and Technology*, 130:1–7, 2016. 1

[12] T. Keravec-Balbot, A. Rodler, L. Roupioz, M. Musy, T. Gresse, and X. Briottet. Identification of urban thermal properties by combining urban microclimate modeling and thermal infrared satellite data. *Sustainable Cities and Society*, 118:105995, 2025. 1

[13] P. A. Mirzaei. Recent challenges in modeling of urban heat island. *Sustainable Cities and Society*, 19:200–206, 2015. 1

[14] William R. Herb, Ben Janke, Omid Mohseni, and Heinz G. Stefan. Ground surface temperature simulation for different land covers. *Journal of Hydrology*, 356(3):327–343, 2008. 1

[15] S Sreedhar and K Prapoorna Biligiri. Development of pavement temperature predictive models using thermophysical properties to assess urban climates in the built environment. *Sustainable Cities and Society*, 22:78–85, 2016. 2

[16] Anabel Palacios, Lin Cong, M.E. Navarro, Yulong Ding, and Camila Barreneche. Thermal conductivity measurement techniques for characterizing thermal energy storage materials – a review. *Renewable and Sustainable Energy Reviews*, 108:32–52, 2019. 2

[17] Rumen K. Krastev. Measuring of heat capacity. *International Journal of Heat and Mass Transfer*, 53(19):3847–3854, 2010.

[18] T.J. Sauer, J.M. Norman, C.B. Tanner, and T.B. Wilson. Measurement of heat and vapor transfer coefficients at the soil surface beneath a maize canopy using source plates. *Agricultural and Forest Meteorology*, 75(1):161–189, 1995.

[19] Pradeep S. Jakkareddy and C. Balaji. A non-intrusive technique to determine the spatially varying heat transfer coefficients in a flat plate with flush mounted heat sources. *International Journal of Thermal Sciences*, 131:144–159, 2018. 2

[20] M.J. Huntul, M.S. Hussein, D. Lesnic, M.I. Ivanchov, and N. Kinash. Reconstruction of an orthotropic thermal conductivity from non-local heat flux measurements. *International Journal of Mathematical Modelling and Numerical Optimisation*, 10(1):102 – 122, 2020. 2

[21] J. Santos, Y. Efendiev, and L. Guarracino. Hydraulic conductivity estimation in partially saturated soils using the adjoint method. *Computer Methods in Applied Mechanics and Engineering*, 196(1-3):161 – 179, 2006. 2

[22] Sultan Alpar, Julien Berger, Bolatbek Rysbaiuly, and Rafik Belarbi. Estimation of soils thermophysical characteristics in a nonlinear inverse heat transfer problem. *International Journal of Heat and Mass Transfer*, 218:124727, 2024. 2

[23] N. Ukrainczyk. Thermal diffusivity estimation using numerical inverse solution for 1d heat conduction. *International Journal of Heat and Mass Transfer*, 52(25):5675–5681, 2009.

[24] K. Yang, T. Koike, B. Ye, and L. Bastidas. Inverse analysis of the role of soil vertical heterogeneity in controlling surface soil state and energy partition. *Journal of Geophysical Research D: Atmospheres*, 110(8):1 – 15, 2005. 2

[25] Julien Berger, Helcio R.B. Orlande, Nathan Mendes, and Sihem Guernouti. Bayesian inference for estimating thermal properties of a historic building wall. *Building and Environment*, 106:327–339, 2016. 2

[26] Zhanat Karashbayeva, Julien Berger, Helcio R.B. Orlande, and Bolatbek Rysbaiuly. Estimation of ground thermal diffusivity using the conjugate gradient method with adjoint problem formulation. *Urban Climate*, 52:101676, 2023. 2, 12

[27] J. Berger and C. Legros. Surface transfer coefficients estimation for heat conduction problem using the bayesian framework. *Heat Transfer Engineering*, 44(5):391–410, 2023. 2

[28] Somchart Chantasiriwan. Inverse heat conduction problem of determining time-dependent heat transfer coefficient. *International Journal of Heat and Mass Transfer*, 42(23):4275–4285, 1999. 2

[29] J. M. Cohard, J.M. Rosant, F. Rodriguez, H. Andrieu, Mestayer P.G., and P. Guillevic. Energy and water budgets of asphalt concrete pavement under simulated rain events. *Urban Climate*, 24:675–691, 2018. 2, 6, 17

[30] Julien Berger, Clemence Legros, and Madina Abdykarim. Dimensionless formulation and similarity to assess the main phenomena of heat and mass transfer in building porous material. *Journal of Building Engineering*, 35:101849, 2021. 2

[31] S. Gasparin, J. Berger, D. Dutykh, and N. Mendes. An improved explicit scheme for whole-building hygrothermal simulation. *Building Simulation*, 11(3):465–481, 2018. 3

[32] H. R. B. Orlande. Inverse heat transfer problems. *Heat Transfer Engineering*, 32(9):715–717, 2011. 4

[33] E. Walter and Y. Lecourtier. Global approaches to identifiability testing for linear and nonlinear state space models. *Mathematics and Computers in Simulation*, 24(6):472–482, 1982. 4

[34] J. Kaipio and E. Somersalo. *Statistical and Computational Inverse Problems*. Applied Mathematical Sciences. Springer New York, 2006. 4, 5, 13

[35] J.V. Beck and K.J. Arnold. *Parameter estimation in engineering and science*. Wiley, 1977.

[36] Daniela Calvetti and Erkki Somersalo. *Introduction to Bayesian Scientific Computing - Ten Lectures on Subjective Computing*. Springer, Germany, 2007. 5

[37] F. Lanzetta and E. Gavignet. Temperature measurements: Thermoelectricity and microthermocouples. *Thermal Measurements and Inverse Techniques*, page 95, 2011. 4

[38] J. P. Kaipio and C. Fox. The bayesian framework for inverse problems in heat transfer. *Heat Transfer Engineering*, 32(9):718–753, 2011. 4

[39] H. R. B. Orlande. Inverse problems in heat transfer: new trends on solution methodologies and applications. *Journal of Heat Transfer*, 134(3):1–13, 2012. 4, 5

[40] F.P. Incropera, D.P. DeWitt, T.L. Bergman, and A.S. Lavine. *Fundamentals of Heat and Mass Transfer*. John Wiley and Sons, England, 6 edition, 2006. 6, 8

[41] M. Mirsadeghi, D. Cóstola, B. Blocken, and J.L.M. Hensen. Review of external convective heat transfer coefficient models in building energy simulation programs: Implementation and uncertainty. *Applied Thermal Engineering*, 56(1):134–151, 2013. 7, 11

[42] John Geweke. Evaluating the accuracy of sampling-based approaches to the calculation of posterior moments. In *Bayesian Statistics 4: Proceedings of the Fourth Valencia International Meeting, Dedicated to the memory of Morris H. DeGroot, 1931–1989*. Oxford University Press, 1992. 14, 15

[43] Marie-Hélène Azam, Julien Berger, Edouard Walther, and Sihem Guernouti. Design and experimental validation of an urban microclimate tool integrating indoor-outdoor detailed longwave radiative fluxes at district scale. *Energy and Buildings*, 347:116370, 08 2025. 21

[44] Rabah Djedjig, Emmanuel Bozonnet, and Rafik Belarbi. Experimental study of the urban microclimate mitigation potential of green roofs and green walls in street canyons. *International Journal of Low-Carbon Technologies*, 10(1):34–44, 04 2013. 22

[45] D.G. Erbs, S.A. Klein, and J.A. Duffie. Estimation of the diffuse radiation fraction for hourly, daily and monthly-average global radiation. *Solar Energy*, 28(4):293–302, 1982. 22

[46] Journal Officiel de la République Française. Arrêté du 26 octobre 2010 relatif aux caractéristiques thermiques et aux exigences de performance énergétique des bâtiments nouveaux et des parties nouvelles de bâtiments, 2010. 22

[47] Moteur de recherche d'archives météo. `www.infoclimat.fr/`. Accessed: 11-01-25. 22